Volume 5
Number 17
7 September 2023
Pages 4301–4612

Nanoscale Advances

rsc.li/nanoscale-advances

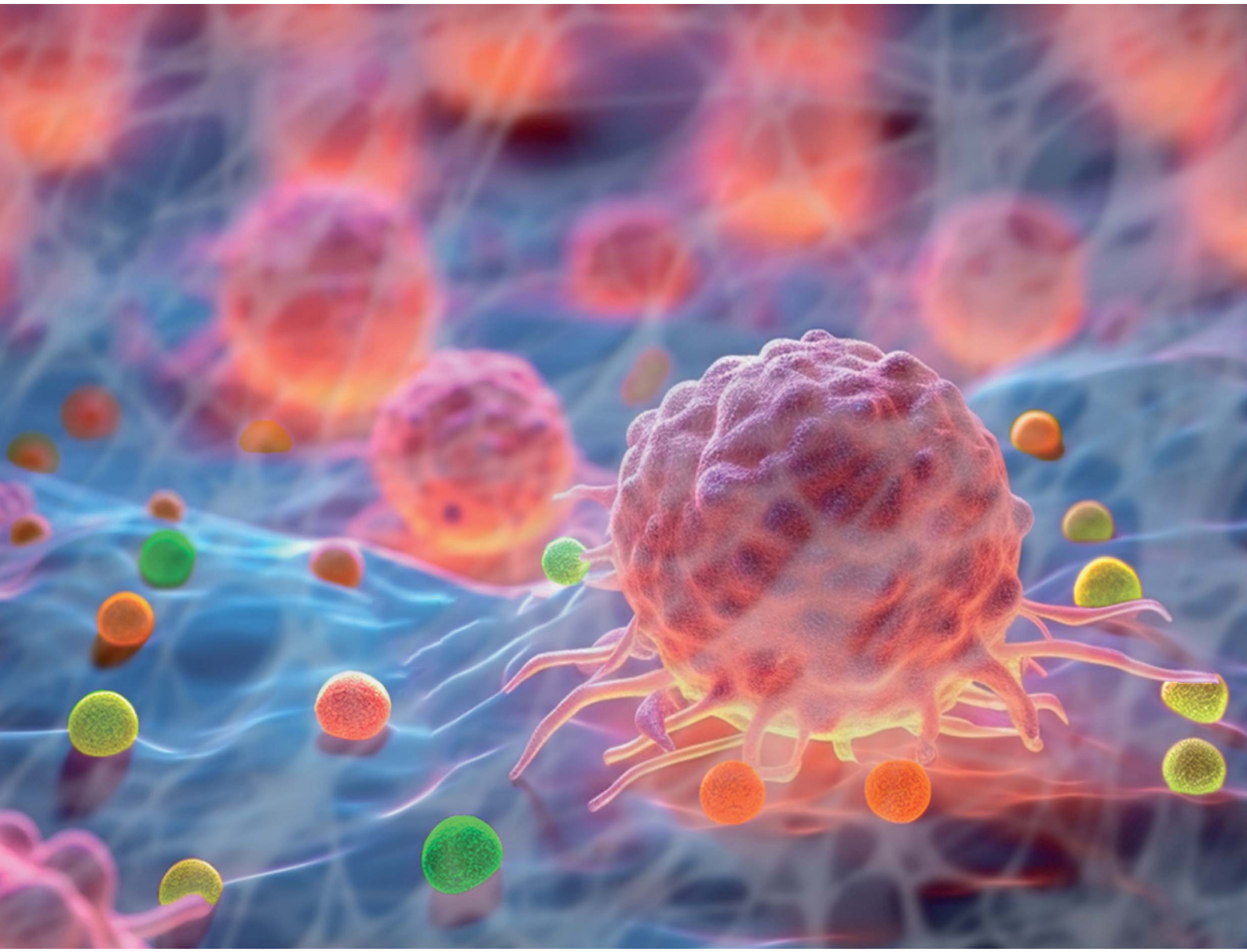

ISSN 2516-0230

ROYAL SOCIETY OF CHEMISTRY

REVIEW ARTICLE

Giuliana Grasso, Loretta L. del Mercato *et al.*

Fluorescent nano- and microparticles for sensing cellular microenvironment: past, present and future applications

NCNST

Nanoscale Advances

ROYAL SOCIETY OF CHEMISTRY

REVIEW

Cite this: *Nanoscale Adv.*, 2023, **5**, 4311

Fluorescent nano- and microparticles for sensing cellular microenvironment: past, present and future applications

Giuliana Grasso,*[a] Francesco Colella,[ab] Stefania Forciniti,[a] Valentina Onesto,[a] Helena Iuele,[a] Anna Chiara Siciliano,[ab] Federica Carnevali,[ab] Anil Chandra,[c] Giuseppe Gigli[ab] and Loretta L. del Mercato *[a]

Received 5th April 2023
Accepted 13th June 2023

DOI: 10.1039/d3na00218g

rsc.li/nanoscale-advances

The tumor microenvironment (TME) demonstrates distinct hallmarks, including acidosis, hypoxia, reactive oxygen species (ROS) generation, and altered ion fluxes, which are crucial targets for early cancer biomarker detection, tumor diagnosis, and therapeutic strategies. Various imaging and sensing techniques have been developed and employed in both research and clinical settings to visualize and monitor cellular and TME dynamics. Among these, ratiometric fluorescence-based sensors have emerged as powerful analytical tools, providing precise and sensitive insights into TME and enabling real-time detection and tracking of dynamic changes. In this comprehensive review, we discuss the latest advancements in ratiometric fluorescent probes designed for the optical mapping of pH, oxygen, ROS, ions, and biomarkers within the TME. We elucidate their structural designs and sensing mechanisms as well as their applications in *in vitro* and *in vivo* detection. Furthermore, we explore integrated sensing platforms that reveal the spatiotemporal behavior of complex tumor cultures, highlighting the potential of high-resolution imaging techniques combined with computational methods. This review aims to provide a solid foundation for understanding the current state of the art and the future potential of fluorescent nano- and microparticles in the field of cellular microenvironment sensing.

1. Introduction

Cancer is one of the leading causes of death globally and has become more widespread over the last several decades owing to unhealthy lifestyles and environmental factors, causing more mutations to happen and increasing the likelihood of cancer development.[1] According to statistical studies recently published by the American Cancer Society, 16.2 million cancer-related deaths and 28 million new cancer cases are projected to be the global burden by 2040.[2,3] Moreover, an event that worsened cancer incidence in the last three years has been the coronavirus disease 2019 (COVID-19) pandemic, which has increased the number of the advanced stage of tumor cases, thereby increasing mortality.[4]

One of the major steps to prevent cancer-associated mortality and increase the chances of successful treatment is the early detection of tumors. To this end, the gold standard methods employed to detect a tumor site are mainly based on medical imaging techniques, where the most common methods are magnetic resonance imaging (MRI),[5] positron emission tomography (PET)[6] coupled to computed tomography (CT),[7] ultrasound scanning,[8] and photoacoustic endoscopy.[9] However, these techniques present some limitations, such as poor compliance from the patient's viewpoint, lack of long-term stability of contrast agents and tracers, and requirement of highly qualified personnel. Together with oncologists, scientists are directing significant resources and efforts towards the study of biological features of tumors that can promote early detection. In this context, the complex TME, in which cancer cells and rich stroma interact with each other releasing growth factors, proteins and membrane-derived vesicles, provides new avenues for early diagnosis.[10–15] Different strategies targeting TME have emerged because of its importance in influencing therapeutic outcomes.[16,17] Notably, TME is highly heterogeneous and dynamic, and it is characterized by the establishment of pH and oxygen gradients resulting from the increased cellular metabolic activity and altered blood perfusion. This marked heterogeneity significantly affects the efficacy of anti-cancer treatments.[18] Dynamic mapping of TME's parameters, such as pH and oxygen, is crucial for understanding their role in cellular and subcellular processes because it can help to better comprehend the link between pH/oxygen distribution, cell

[a]*Institute of Nanotechnology, National Research Council (CNR-NANOTEC), c/o Campus Ecotekne, via Monteroni, 73100, Lecce, Italy. E-mail: giuliana.grasso@nanotec.cnr.it; loretta.delmercato@nanotec.cnr.it*

[b]*Department of Mathematics and Physics "Ennio De Giorgi", University of Salento, c/o Campus Ecotekne, via Monteroni, 73100, Lecce, Italy*

[c]*Centre for Research in Pure and Applied Sciences, Jain (Deemed-to-be-university), Bangalore, Karnataka 560078, India*

morphology, and cell functions. In this context, numerous sensing systems have been developed to facilitate the prompt detection of key analytes in the TME and to obtain a valid metabolic read out for cancer diagnosis and treatment.[19,20] Among these, ratiometric fluorescence-based nano- and microsensors stand out as valid and non-invasive approaches for characterizing cellular microenvironments and sub-cellular compartments with high precision over time and space. These technologies pave the way for the powerful era of modern precision and personalized medicine.

1.1 Deep insight into TME

The genesis and the development of cancer diseases involve multistep processes that start with genetic or epigenetic changes in tumor cells,[21–23] followed by dynamic crosstalk, leading to the rearrangement of a tumor-supportive and highly reactive microenvironment (TME) that surrounds the tumor (Fig. 1).[24–26] It is now widely recognized that TME plays a crucial role in cancer initiation,[27] progression[28] and metastasis.[29]

The main constituents of the TME are cancer cells[30,31] and accessory cells, including cancer-associated fibroblasts (CAFs),[32,33] immune and inflammatory cells,[34,35] all of which are embedded in a dense stroma of extracellular matrix (ECM) components, such as collagen type I,[36,37] fibronectin,[38] hyaluronic acid[39] and growth factors.[40] ECM not only functions as a support for tumor cells but also regulates and promotes cell–cell and cell–matrix interactions.[41] Additionally, the ECM is involved in signalling pathways that regulate cell behaviour and differentiation; therefore, changes in the ECM can disrupt normal cellular processes, leading to disease development and progression.[42] Thus, the interplay between cancer cells and ECM contributes to the increase in tumor heterogeneity, which is considered the major cause of treatment failure in current therapies.[43] This feature is not only a consequence of clonal outgrowth of cells with genetic alterations but also of epigenetic alterations promoted by several physical and biochemical signals from the TME.[44] The unlimited multiplication of tumor cells is a phenomenon strictly related to their ability to elude growth suppressors[45] and apoptotic signals.[46] As a result, the TME promotes a sequence of physical (acidosis, hypoxia, temperature and stiffness)[47,48] and biochemical (adhesion proteins, glycoproteins and proteoglycan, secreted factors, growth factors, and matrix degradation enzymes)[49] adaptations that promote angiogenesis,[50] invasion[51] and metastasis.[52] Moreover, to survive in a hostile microenvironment, which is characterized by high deprivation of oxygen and nutrients, and to maintain a high proliferative rate, some tumor cells are known to adjust their metabolism,[53,54] from the oxidative phosphorylation towards the aerobic glycolysis, the so-called "Warburg effect",[55] which was first observed by Otto H. Warburg in the early twentieth century.[56] In normal cells with adequate oxygen levels, the pyruvate produced by the breakdown of glucose during the glycolysis process and could enter into the tricarboxylic acid (TCA) cycle to generate energy.[57]

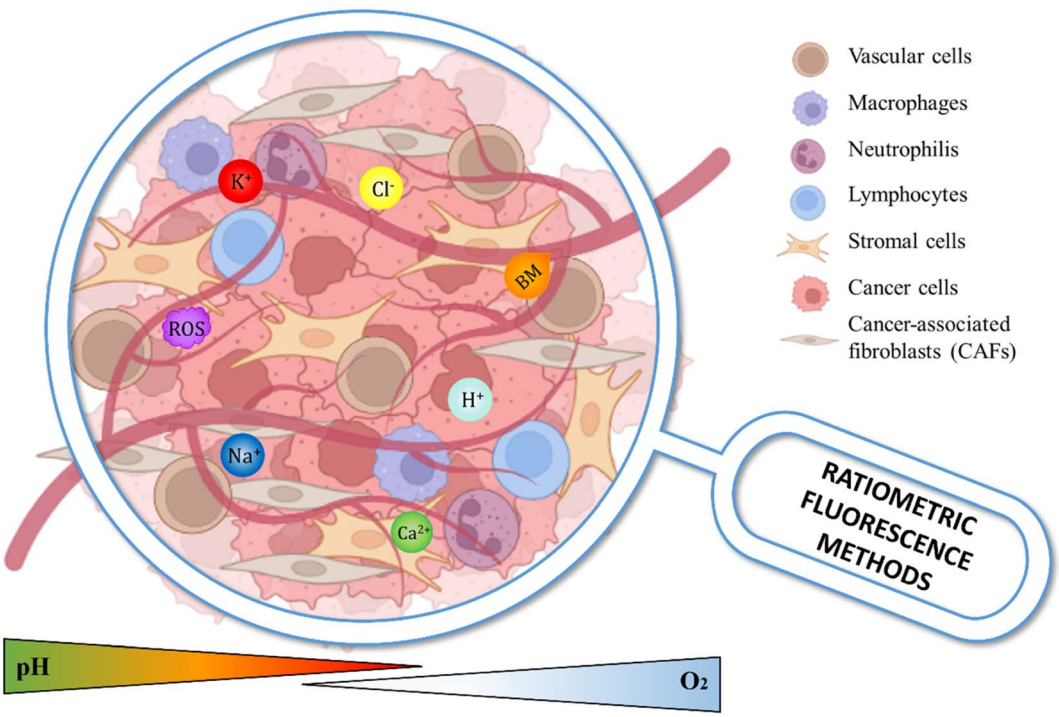

Fig. 1 A close-up look at the different characteristics and analytes having a biological significance within the TME, which can be precisely examined by ratiometric fluorescence methods. The heterogeneity of the TME is mainly due to the complex ecosystem created by the interactions among tumor, stromal and immune cells, all of which are immersed in a dense and dysregulated ECM. Poor blood flow and crowded glycolytic tumor cells form niches characterized by reduced oxygenation, pH acidity, reduced nutrient loading, collection of anti-inflammatory cytokines and chemokine, and storage of metabolic by-products, such as lactate.

Tumor cells instead exhibit increased glycolysis activity regardless of the amount of oxygen and produce lactate by activating lactate dehydrogenase and inhibiting mitochondrial metabolism.[55] The resulting acidosis effect is a direct consequence of lowering of extracellular pH from physiological pH 7.4 to values up to 5.0, whereas the intracellular pH is increased compared to that of normal cells. Consequently, the acidity of the interstitial space and the high intracellular pH affect the dynamic and functional cell–cell or cell–matrix crosstalk.[58] The low extracellular pH is an important factor for inducing more aggressive cancer phenotypes, increasing cell motility, extracellular matrix degradation and modifying cellular and intercellular signaling.[59,60] Furthermore, the accumulation of protons (H^+) in the extracellular environment is spatially and temporally heterogeneous and influences the efficacy of chemotherapeutic treatments.[61] Additionally, it has been well established that also intracellular pH is dysregulated in cancer.[62,63] Although many biological mechanisms contribute to intracellular pH dynamics, the main regulators are the plasma membrane ion exchangers, such as Na^+/H^+ exchanger 1 (NHE1), and plasma membrane ion transport proteins, including V-ATPases and the monocarboxylate transporters (MCTs). Changes in their expression and activity to facilitate H^+ efflux contribute to maintaining alkaline intracellular pH and acidic extracellular pH in tumor cells.[64]

Furthermore, the higher intracellular pH promotes many cancer behaviors, such as increased proliferation, migration, epithelial plasticity and the oncogenic and tumor suppressor functions of mutated proteins.[65] Notably, in solid tumors, the low vascularization due to impaired vascular network with the formation of abnormal blood vessels and the reduced perfusion of oxygen within the TME equally contribute to the metabolic switch of the cancer cells, promoting the acidification of the TME.[66] This phenomenon known as hypoxia is mainly induced by hypoxia-inducible factors (HIFs), which are recognized as master regulators of cell metabolism.[67] The reduction of oxygen levels in the TME is associated with angiogenesis activation and increasing tumor survival, invasiveness, and metastatic potential and hampers the therapeutic response.[68]

The hypoxic microenvironment also induces the expression of genes that sustain tumor progression and the generation of reactive oxygen species (ROS).[69] 'Reactive oxygen species' term groups together two classes of molecular oxygen products derived from reduction–oxidation reactions or electronic excitation during aerobic cellular respiration, which are namely non-radical and free radical species. Examples of ROS are hydrogen peroxide (H_2O_2), its reduction product hydroxyl radical ($^{\bullet}OH$), and superoxide anion radical ($O_2^{\bullet -}$).[70–72] These side products derived from cellular respiration and carried out in mitochondria under physiological conditions are kept under control by detoxification mechanisms.[73,74] The maintenance of their concentration within physiological levels (10^{-8} M for H_2O_2 and 10^{-11} M for $O_2^{\bullet -}$) is called oxidative eustress.[75] In this phenomenon, more than 40 enzymes, particularly NADPH oxidase enzymes, are involved in the redox signalling pathways that promote proliferation, differentiation, migration and angiogenesis.[76] In contrast, elevated levels of ROS in the cellular microenvironment determine oxidative distress, a condition in which unspecific protein oxidation leads to reversible or irreversible damages of biomolecules, causing pathological states that include inflammation, tumor growth, metastasis and cell death.[77] In the cancer field, the study of ROS has attracted increasing interest in the last twenty years because it is now generally recognized that the regulation of oxidative stress represents a key factor of tumor development and its responses to anticancer therapies. Gorrini's group[78] remarked that moderate concentrations of ROS may contribute to tumor progression because they act as signalling molecules and promote the mutation of nuclear DNA and mitochondrial DNA (mt-DNA). Moreover, concomitant conditions in the TME, such as hypoxia, metabolic defects inducing the Warburg effect,[79] endoplasmic reticulum (ER) stress, and activation of oncogenes, cooperate to produce a significant increase in ROS concentration.

In healthy cells, inorganic ions can play different roles in the homeostasis of the human body. For instance, inorganic metal cations, such as magnesium (Mg^{2+}), zinc (Zn^{2+}), iron (Fe^{2+}) and copper (Cu^{2+}), are essential in enzymatic reactions by acting as cofactors, while the cations calcium (Ca^{2+}), sodium (Na^+) and potassium (K^+), and the anion chloride (Cl^-) is involved in electrophysiological events.[80] During the malignant transformation of healthy cells into cancer cells, mutations of genes also affect those encoding for plasma membrane ion channels, thus resulting in the alteration of the ion fluxes, cell membrane potentials (V_{mem}), and, consequently, modifications in the intracellular signalling pathways.[81–83] The disruption of ion homeostasis, about the transport of ions through channels and their concentration within the TME, yields biophysical phenomena, such as elevated pressure, increased stiffness, and mechanical stress. Subsequently, these alterations lead to the activation or attenuation of molecular signaling pathways implicated in cancer initiation, promotion, and invasion processes.[84] One indicator of normal cells transitioning into cancerous and proliferative tissues is the more positively charged or depolarized membrane, with a V_{mem} increasing from −60 mV to −10/−30 mV in more undifferentiated cancer stem-cells.[85,86] The cytosolic Ca^{2+} levels are important for the integrin-signalling pathway, which is activated to facilitate cell–cell and cell–ECM communication. The cytosolic Ca^{2+} levels are important for the integrin-signalling pathway, which is activated to allow cell–cell and cell–ECM communication. The dysregulation of calcium ions within cells contributes to cancer-related processes. In particular, intracellular Ca^{2+} concentration plays a crucial role in regulating cytoskeletal dynamics, which are involved in extracellular matrix (ECM) degradation and the initiation of the metastatic process. This occurs through the activation of epithelial–mesenchymal transition (EMT) pathways and the enzymatic activity of metalloproteases.[87,88] Strictly linked to Ca^{2+} functions are the fluxes of Na^+ cations, which are involved in the synergistic activity of Na^+/Ca^{2+} exchangers.[89] Furthermore, alterations in intracellular Na^+ concentrations lead to a reduction in H^+ in the vicinity of cancer cells, resulting in the formation of integrin-mediated focal adhesion contacts that promotes cell adhesion.[90] Concomitant with alterations in

the membrane potential of cancer cells, K^+ fluxes are linked to proliferation, as fluctuations in K^+ levels interact with extracellular signal-regulated kinase (ERK 1/2) and c-Jun N-terminal kinase (JNK) signalling pathways.[91,92] Additionally, the Cl^- anion, which typically facilitates the transport of cations, such as Ca^{2+}, Na^+, and K^+, can promote migration and metastasis by modulating cell volume.[93]

1.2 Fluorescent ratiometric sensors for TME investigation and mapping

Understanding the mechanisms underlying cell–cell interactions is essential for mapping the tumor microenvironment (TME), which is currently a critical aspect of improving prognosis, diagnosis, and therapies. In this context, nanotechnologies aimed at precision medicine pave the way for a groundbreaking approach to combating cancer. This is due to their extensive applications in detecting signature biomarkers, which are crucial steps toward early diagnosis and targeted therapeutic drug delivery.[94] Optical biosensors, particularly those based on fluorescence (FL), are becoming increasingly important in cancer research owing to their enhanced detection capabilities. They represent valuable tools for detecting and analysing a wide range of biomolecules, making them advantageous for studying cancer-related processes.[95] Fluorescence microscopy is a critical tool for bio-imaging and optical sensing of specific analyte concentrations in tissues and cancer models,[96] where the most commonly used fluorescence microscopy techniques include fluorescence lifetime imaging microscopy (FLIM),[97] phosphorescence lifetime imaging microscopy (PLIM),[98] and near-infrared (NIR) microscopy.[99] The methods mentioned earlier require specialized and sophisticated equipment, but the introduction of ratiometric fluorescence (FL) measurements has significantly improved the performance of fluorescence microscopy applications.

Ratiometric FL enables the precise measurement of analyte concentrations within the TME, making it an increasingly valuable tool in cancer research. Many research groups have focused on the achievement of responsive FL molecular probes to detect single targets within the TME. For example, Anderson *et al.* developed a ratiometric pH-sensitive fluorescent dye based on a seminaphtharhodafluor (SNARF) core to compare the surface cell pH of cancer cells grown either in spheroids, mouse tumor models or in excised tumors.[100] In a different approach, Zheng *et al.* employed an iridium-based hypoxia-activated optical molecular probe to produce an oxygen nanosensor suitable to perform hypoxia imaging in mice bearing hepatoma cells, H22.[101,102] Recently, the possibility of detecting two cancer parameters at the same time within the TME has provided the opportunity to deeper correlate cancer hallmarks with each other. In the same research group, Zheng and collaborators designed and synthesized an ultrasensitive molecular probe based on a poly(ethylene glycol)-conjugated iridium(III) complex (Ir-Im-PEG). The imaging of tumor acidity and hypoxia, carried out simultaneously, was studied and performed both *in vitro* using the HeLa cell line and *in vivo* by implanting H22 tumors subcutaneously in mice.[103] In a different study, Yeh and co-workers successfully employed commercially available probes, SNARF-1 and Rhod-5N, to map and quantify protons and calcium concentrations using an imaging approach. The data obtained allowed the correlation of pH and calcium levels in the intravascular and interstitial space of bone marrow in the mouse calvarium.[104] Thus, sensing FL analytical platforms are among the most used tools because they permit the investigation of the physiological and pathological processes of living organisms.[105–107] Many of them have been developed and act as indicators for monitoring and quantifying specific analytes and clinically relevant metabolites.[108,109]

Despite advancements in fluorescence-based sensor technology, designing sensors for *in vitro* and *in vivo* applications remains a challenging task because of numerous factors to consider, such as sensor selectivity, sensitivity, biocompatibility, and stability.[110] The vast potential of particle-based systems in elucidating the intricacies of the TME is due to the infinite possibilities of tuning materials, size, shape, surface charge, and functionalities, coupled with their ease of preparation and, in some cases, intrinsic biocompatibility. Silica (SiO_2), polystyrene (PS), and poly(methyl)methacrylate (PMMA) nanoparticles are particularly noteworthy owing to their large specific surface area, stability properties, and viability. These features make them attractive candidates for *in vitro* and *in vivo* applications in cancer research.[111,112] Additionally, the coupling of fluorescence (FL) molecular probes to structured micro- and nano-systems has garnered significant interest owing to their high analyte sensitivity, low cost, and rapid spatiotemporal resolved measurements. The unique features of nanoparticles make them ideal for studying various cancer-related processes, such as bio-imaging and optical sensing of oxygen concentration in tissues and cancer models using fluorescence microscopy, particularly FLIM. Organic dyes with specific excitation and emission wavelengths can serve as probes to reliably respond to specific targets in the TME, making them valuable tools for cancer research. The FL behaviour of the molecular probe is determined by structural changes in the fluorophores resulting from the formation and/or breakdown of responsive functional groups. These changes can cause FL quenching (off) or FL enhancement (on) effects,[113] which are the results of Förster Resonance Energy Transfer (FRET), photoinduced energy transfer (PET), internal charge transfer (ICT), and self-quenching phenomena. Understanding these phenomena is crucial for developing effective molecular probes for various applications in cancer research. Although single dye-doped sensors are widely used and easily manipulated, they often lack accuracy owing to instrumental, operational, and environmental variations that can interfere during analyses. To address this issue, single-signal sensors have been replaced with ratiometric FL sensors. These sensors incorporate a second FL target-insensitive signal that serves as a reference signal, reducing the possibility of errors through self-calibration and refining the detection limits of the sensors. This advancement has significantly improved the accuracy and reliability of molecular probes used in cancer research.[114,115] Another strategy to build a ratiometric FL-sensor is the employment of a dual-emissive probe, which presents two reversible detection

signals that are strictly interrelated (Fig. 2). Thus, as a general rule, ratiometric analysis is calculated by plotting the ratio of two FL signals. Moreover, the encapsulation of dyes within the matrix of biosensors can improve the performance of the developed analytical platforms in terms of target selectivity. There are still some aspects that represent current challenges regarding environmental perturbations over long-time experiments, photobleaching, and light scattering phenomena. Within the vast world of nanosized-photoluminescent particles, it is possible to identify two main categories: quantum dots and metallic nanoclusters.[116] The multiple advantages observed in the field of fluorescence imaging over the last few years mainly stem from the discovery and the development of brilliant nanoparticles, which are synthetically obtained using elements from groups II–VI, IV–VI and III–V of the periodic table *via* different techniques.[117–119] These nanoparticles, with quantum confinement effects, are defined as semiconductor nanocrystals or simply quantum dots (QDs). Single properties, such as size-dependent emission, narrow emission peaks, and resistance to photobleaching, promote the achievement of optical sensing systems based on QDs compared with the use of organic dyes.[120] However, biosensing systems exploiting QD potentials must overpass their cytotoxicity in biological systems[121] by surface modifications and/or coating with biocompatible materials.[122–124] Moreover, metallic nanoclusters (MNCs), metal-centred nanoparticles that can be stabilized by protective groups, usually biological molecules, represent powerful alternative platforms for fluorescence sensing *in vitro* and *in vivo*, and their investigation has been growing over the years. Among their properties, it is important to note intrinsic water solubility and biocompatibility.[125,126]

In this comprehensive review, we delve into cutting-edge developments in the detection and monitoring of critical TME parameters, including pH, O_2, ROS, and inorganic ions, along with crucial tumor biomarkers. Through the implementation of nano- and microparticle-based ratiometric fluorescence sensors, we present an in-depth analysis of their latest integrations in two- and three-dimensional architectures. Our review includes a detailed description of the intricate mechanisms behind these sensors and showcases their impressive *in vitro* and *in vivo* applications while providing an insightful analysis of the strengths and limitations of each system.

2. Microenvironment parameters under study

2.1 pH

The real-time monitoring of pH in the biological environment is a challenging task[127] that cannot be fulfilled by standard methods. In lab practice, the pH-meter electrodes used are cheap and reliable tools for bulk pH measurements, but the difficult miniaturization of these devices makes them less suitable for *in vitro* and *in vivo* studies. From a physiological viewpoint, proton (H^+) concentration varies from one cellular compartment to another. For instance, pH in the cytosol has

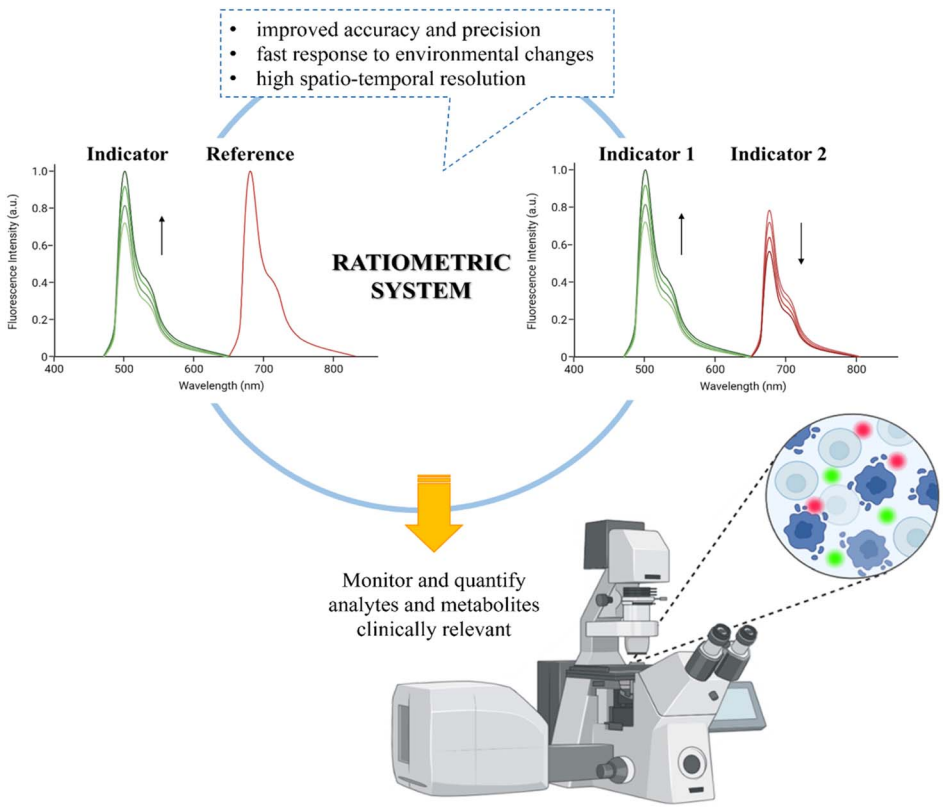

Fig. 2 Sketch of the ratiometric optical methods with their advantages and applications in sensing TME *in vitro* and *in vivo*.

a value in the range of 7.0–7.4, and it is among 7.2 in the endoplasmic plasmatic reticulum (ER), while it is slightly acidic in the organelles, as it is 6.4 in the Golgi apparatus, 5.0 in lysosomes, 5.4 in secretory granules, 6.2 in early endosomes, 5.3 in late endosomes, and 8.0 in mitochondria.[84,128–130] The metabolic switch induced in cancer growth breaks the balance between the compartments of cells, determining pH fluctuations not only in the intracellular environment but also in the extracellular surrounding. Therefore, the need of monitoring and mapping pH inside the cells and in the space between cells constitutes a crucial topic of research interest. Consequently, FL small molecules and nanoprobes have been intensively developed and studied for sensing pH.[131] Optical pH measurement is based on the significant change in absorption or fluorescence of suitable pH indicators after protonation/deprotonation at different pH values. Today, many fluorescent pH indicators are commercially available (*e.g.*, fluorescein, seminaphtharhodafluor 1 (SNARF1), 8-hydroxypyrene-1,3,6-trisulfonic acid trisodium salt (HPTS), and Nile Blue A), and most of them have been successfully employed in non-invasive and real-time imaging of pH in several physio-pathological processes.[132] However, one of the main challenges of pH-sensing molecules is their limited sensitivity range and, for some of them, lack of solubility in water solutions, as well as toxicity. Therefore, the encapsulation of FL pH-sensing molecules into nano-structured and biocompatible matrices improves the final analytical platform in terms of photostability, solubility and cell viability, thereby enhancing accuracy. Striking examples are the polyelectrolyte multilayer capsules obtained *via* the layer-by-layer (LbL) method, which in the past two decades have irrupted the scene of nanotechnology as a straightforward and versatile technique.[133–135] In 2011, del Mercato employed the dual-emission ratiometric SNARF1-dextrane derivate to prepare permeable calcium carbonate ($CaCO_3$)-based capsules using the LbL technique.[136] The ratiometric SNARF1 dye has the unique property of displaying two emission peaks, depending on pH: the excitation at 543 nm determines, at acidic pH, an emission peak with a maximum value at 594 nm, while, in basic pH, a spectral emissive band at 640 nm is recorded. The FL characterization, employing spectroscopy and FL microscopy, carried out on the pH sensing capsules, confirmed the ability of the labelled and encapsulated amino-dextran SNARF1 ($\lambda_{ex} = 543$ nm, $\lambda_{em1} = 594$ nm; $\lambda_{em2} = 640$ nm) to efficiently sense H^+ concentrations with the same sensitivity as the free dye. Later, the same capsules were applied to measure the intracellular pH in MCF-7 breast cancer cells. The cellular uptake of capsules was tracked to monitor pH in the endosomes and lysosomes.[137,138] In a different approach, multilayer pH-sensing capsules, based on SNARF probe, were successfully applied to map the pH microenvironment of human mesenchymal stromal cells (hMSCs) seeded in 3D additive manufactured scaffolds.[139] A fully automated computational approach for precisely measuring organelle acidification in cancer cells was set up by Chandra and colleagues.[140] The authors developed micrometer-sized silica (SiO_2) particles that were functionalized with fluorescein 5-isothiocyanate (FITC) ($\lambda_{ex} = 492$ nm; $\lambda_{em} = 518$ nm), as pH probe, and rhodamine B isothiocyanate (RBITC) ($\lambda_{ex} = 570$ nm; $\lambda_{em} = 595$ nm), as the reference dye. Furthermore, to ensure internalization in the cytosolic comportment, the MPs were decorated with a net positive external charge that allowed cell uptake and the finest acidic sensing property because of the lowered pK_a (6.30 ± 0.09). The tracking and mapping experiments were performed by applying CLSM time-lapse using tumor models MDA-MB-231 and MCF-7 breast adenocarcinoma cell lines (Fig. 3a). The innovation of the entire method depended on the automated computational approach, which simplified and enriched the interpretation of data derived from image acquisitions through the creation of *ad hoc* algorithms.

Over the last decade, many groups have developed new FL probes with a wider range of sensitivity towards pH values. This is the case developed by Srivastava and collaborators[141] who recently synthesized a novel pH-responsive green naphtalimide-based dye ($\lambda_{ex} = 405$ nm; $\lambda_{em} = 525$ nm) (Fig. 3b). The dye was obtained by covalently linking two functional moieties: a selective lysosomal targeting part, represented by a morpholine unit bound to 4-bromo-1,8-naphthalic anhydride, and a piperazine ring, which improves the solubility of the dye in water. The working mechanism of the pH-sensing dye was studied over all pH ranges. In detail, the protonation of the morpholine and piperazine amine groups determined the switch-on in an acidic environment of the green FL signal, which therefore was PET-induced quenched gradually passing across neutral and basic pH, thus characterizing the probe selectivity ranging from 2.0 to 8.0 pH values. The significance of this study depends on the fabrication of ratiometric SiO_2 NPs, coupling the reference RBITC dye ($\lambda_{ex} = 570$ nm; $\lambda_{em} = 595$ nm) to the green synthesized pH-indicator dye, and their subsequent *in vitro* application for mapping lysosomal uptake and pH fluctuations in the human lung cancer A549 cell line using CLSM. Although the developed analytical platform has demonstrated its suitability for this purpose, the authors acknowledge the need for deeper live-cell imaging studies, specifically regarding the co-localization of the NPs in the endosomes and lysosomes. These studies are crucial for further validating the effectiveness of this innovative approach in cancer research.

Although pH-sensitive fluorescent nanosensors based on hydrophobic indicators are largely unexplored, boron-dipyrromethene (BODIPY) and boron-azadipyrromethene (aza-BODIPY)-based dyes are noteworthy examples. The introduction of hydrophilic moieties to the BODIPY core has significantly enhanced their water solubility while retaining their fluorescence properties.[142] Currently, near infrared (NIR) emissive aza-BODIPY pH-indicator compounds were synthesized by Strobl *et al.* and were presented as novel dyes covering the pH scale ranging from 1.5 to 13.[143] The great advantages of using such types of dyes in long-wavelength spectral regions are the enhanced photostability, less scattering background and deep light penetration. Despite several *in vitro* and *in vivo* studies of BODIPY dyes,[144] the biotechnological development of ratiometric pH platforms and their further applications in cell sensing are not present in the literature. However, the successful engagement of hydrophobic pH-sensing dye chromoionophore III (Ch3 or ETH 5053) for exploring lysosomal pH

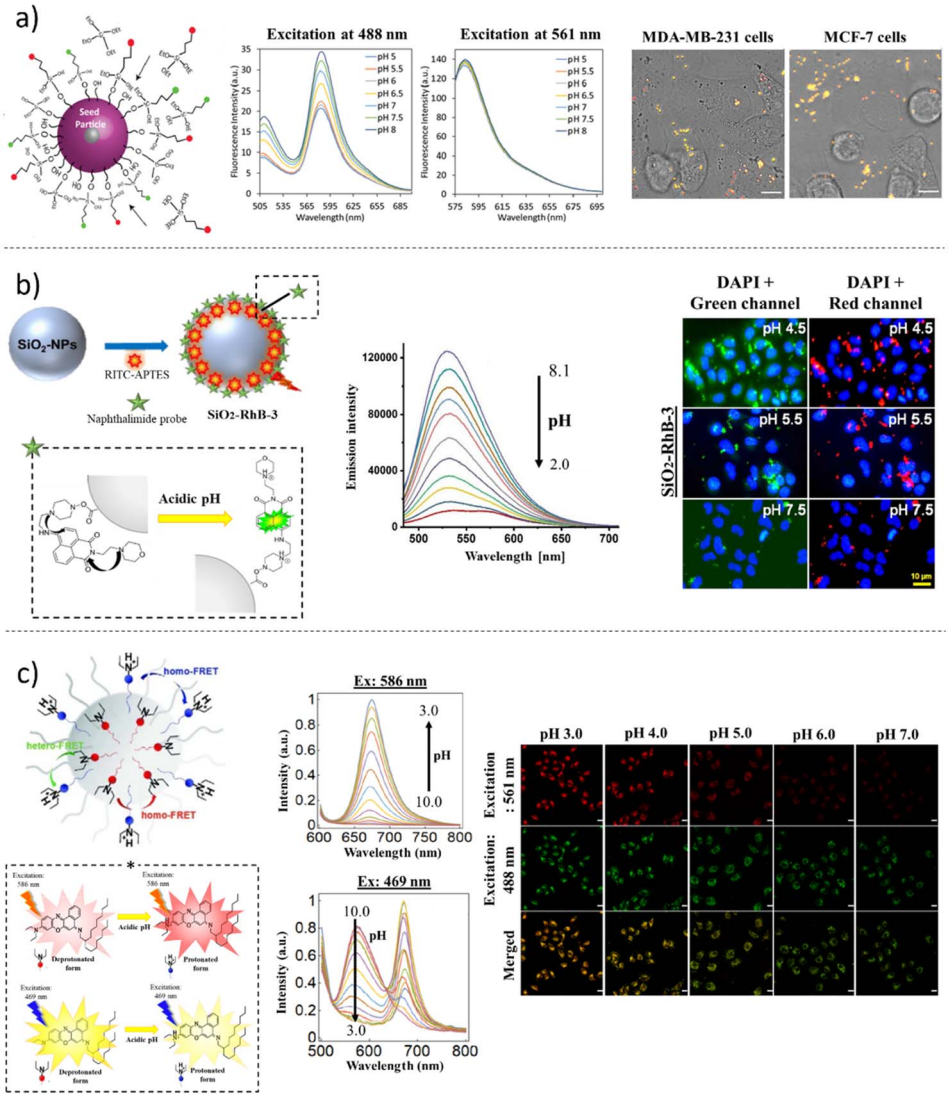

Fig. 3 Examples of pH sensing ratiometric nano-platforms. (a) (Left): Schematic illustration of the ratiometric SiO_2 MPs functionalization with FITC and RBITC dyes using a modified Stöber method; (middle): pH-dependent fluorescence of the MPs; (right): fluorescence micrographs showing the color changes in the ratiometric pH-responsive MP sensors added to MDA-MB-231 cells and MCF-7 cells after incubation for 24 hours. Scale bars: 10 μm. Adapted with permission from Chandra *et al.*, *ACS Appl. Mater. Interfaces* 2022, **14**, 18133–18149; figure licensed under CC-BY 4.0, https://creativecommons.org/licenses/by/4.0/. (b) (Left): Schematic representation of the protocol used to synthesize pH-sensing SiO_2-NPs; (middle): pH-dependent fluorescence of probe 3 on NPs; (right): epifluorescence images of fixed A549 cells incubated with solutions of pH nanosensors SiO_2–RhB-3, monitoring with emission filters set to $\lambda_{em} = 470$ nm (green channel) and to $\lambda_{em} = 560$ nm (red channel). Scale bar: 10 μm. Adapted with permission from Srivastava *et al.*, *Sci. Rep.*, **13**, 1321, 2023; figure licensed under CC-BY 4.0, https://creativecommons.org/licenses/by/4.0/. (c) (Left): Schematic illustration and working principle of the protonation of Ch3 at the surface of the NPs, turning the color from red to blue; (middle): fluorescence emission spectra (excitation at 586 nm) of the nanosensors containing Ch3, PS-PEO, and NPOE in universal buffer solutions at different pH values from 10 to 3, upon excitation at 586 and 469 nm; (right): CLSM images for the cellular pH calibrations of the nanosensors from pH 3.0 to 7.0. Scale bar: 20 μm. Reprinted with permission from Chen *et al.*, *Nano Res.*, 2022, **15**(4): 3471–3478. Copyright © 2021, Tsinghua University Press and Springer-Verlag GmbH Germany, part of Springer Nature.

was published by Chen and collaborators in 2022 (Fig. 3c).[145] The authors reported the encapsulation of hydrophobic Nile Blue A-derivate Ch3 into the polymeric matrix of poly(styrene)-graft-poly(ethylene oxide) (PS-PEO) NPs. Ch3 is a ratiometric pH sensing probe characterized by two excitation wavelengths and emissive spectra in the far-red region ($\lambda_{ex1} = 586$ nm and $\lambda_{em1} = 675$ nm; $\lambda_{ex2} = 469$ nm and $\lambda_{em2} = 575$ nm), corresponding to the protonated and deprotonated forms, respectively. The mechanism of FL emission is regulated by the FRET phenomenon: moving from pH 10 to 3, the emission peak at 575 nm gradually decreases upon excitation at 469 nm, whereas *vice versa*, the emission peak at 675 nm gradually increases. The linear regression recorded by plotting the FL intensity at 675 nm *versus* the FL intensity at 575 nm enabled the authors to test the pH nanosensors, followed by incubation with HeLa cells. The Ch3-NPs were endocytosed by HeLa cells,

and subcellular pH monitoring was carried out using time-lapse CLSM acquisitions. After proper pH calibration of the sensors, carried out in the cell medium, the pH of the organelles was determined to be approximately 4.7. The sensor system proposed by Chen and colleagues[145] greatly summarized the potential of ratiometric NP engineering, highlighting the easy preparation through dye embedding in a biocompatible matrix, thus making the system suitable for future *in vitro* and *in vivo* applications.

2.2 Oxygen

The hypoxia switch-on represents a hallmark within the TME that leads towards concomitant events, such as the metabolic switch, acidosis and ECM rearrangement phenomena, which in turn are involved in the progression and MDR of cancer.[146] Therefore, considering the variations of the partial pressure of oxygen (ppO_2) appears as the main strategy to be monitored, both *in vitro* and *in vivo*.[147] Nowadays, several methods for the detection of dissolved oxygen concentration are widely published in the literature, and they are based mainly on electrochemical (amperometry, potentiometry, or conductometry) and chemical (Winkler titration) techniques.[148] Although various methods for sensing TME parameters exist, they often lack dynamic real-time and spatiotemporal resolution at a single-cell scale. However, in recent decades, optical and ratiometric FL probes have become the preferred methodology for bioimaging applications, and the field has exhibited increasing advancements. The principle behind oxygen sensing relies on the quenching of the luminescence intensity of an indicator probe by molecular oxygen (O_2), a phenomenon governed by energy or electron transfer mechanisms that are well described in the Stern–Volmer equation. By utilizing such probes, researchers may gain valuable insights into oxygen levels within the TME, which may have important implications for the development of novel diagnostic and therapeutic approaches in cancer research.[149] Moreover, another important parameter to consider is the diffusion coefficient (D) of O_2 throughout the matrix in which the indicator is immersed. Thus, the combination of the choice of the optimal oxygen sensing indicator, together with an unquenchable and photostable reference dye, and the selection of the suitable, inert and gas-permeable/ion-impermeable matrix enable the fabrication of O_2 ratiometric FL sensing devices. In this portrait, various oxygen-permeable materials (silicon polymers, organic glassy polymers, fluoropolymers and cellulose derivate polymers)[150,151] and reversibly quenched oxygen indicator probes (*e.g.* transition metal polypyridyl complexes and metalloporphyrins)[152] are commercially available.

Among all the transition metal dyes, ruthenium (Ru(II))-based polypyridyl complexes are extensively adopted in bioimaging applications owing to their properties, such as large Stokes' shift, excitation and emission band in the visible region, good photostability and high brightness.[153] Despite these characteristics, the excitation and the emission peaks remain quite broad, which can be interpreted positively, having more possibility of choice for the laser excitation, or negatively, because of the difficulties in isolating the emission band during multi-analyte measurements.[152] However, (Ru(II))-based polypyridyl complexes remain the most used O_2-molecular probes. For instance, Xu *et al.* reported in 2001 the first sol–gel-based ratiometric FL PEBBLEs for the real-time measurements of oxygen in rat C6 glioma cell line.[154] The nanosensor was built-up by encapsulation within the matrix of silica particles, obtained by a modified Stöber method, of the indicator and reference dyes, which were ruthenium(II)–tris(4,7-diphenyl-1,10-phenanthroline) dichloride ($[Ru(dpp)_3]^{2+}$) (λ_{ex} = 543 nm; λ_{em} = 610 nm) and Oregon Green 488-dextran (λ_{ex} = 488 nm; λ_{em} = 525 nm), respectively. The ratiometric linear regression plot, obtained from the calibration curve at different rates of O_2, allowed the authors to inject the ratiometric FL nanoprobes into rat C6 glioma cells and collect preliminary information regarding intracellular oxygen through CLSM image acquisition. At that time, the novelty of the work published was the first development and application of a ratiometric O_2 sensing system; however, the platform possessed a great limitation, which was the absolute need to control pH within the cell medium because Oregon Green is a pH-sensitive dye for pH values below 6.0.

Platinum (Pt(II))- and palladium (Pd(II))-based metalloporphyrins constitute another category of optical O_2 sensors having strong phosphorescence, good molar absorption coefficients and large Stokes' shifts.[155] In the work reported by Wu and collaborators, platinum(II)-octaethyl porphyrin (PtOEP) (λ_{ex} = 580 nm; λ_{em} = 650 nm) was employed as oxygen sensitive dye and entrapped using particle precipitation technique into the matrix of polyfluorene derivates poly(9,9-dihexylfluorene) (PDHF) (λ_{ex} = 350 nm; λ_{em} = 420 nm) and poly(9,9-dioctylfluorene) (PFO) (λ_{ex} = 350 nm; λ_{em} = 420 nm), which in turn acted as reference signals in the ratiometric system and as hydrophobic, glassy and gas-permeable polymers.[156] The working mechanism of the probes was based on the FRET phenomenon, in which the PDHF and PFO were the donor units, whereas PtOEP was the acceptor one. In this study, π-conjugated polymer nanoparticles (CPdots) exhibited peculiar properties: under excitation, the polymer matrices were capable of transferring energy to the phosphorescent PtOEP, thus enhancing its sensitive ability to respond at different concentrations of oxygen; additionally, the confinement inside the polymeric matrices determined augmented photostability. Therefore, the fluorescence emission of PtOEP was linearly quenched in the presence of increasing concentrations of O_2, while PDHF and PFO did not change their fluorescence signals. Following the characterization of the sensors, the authors tracked the cellular uptake operated by the macrophage-like murine J774A1 cell line using differential interference contrast (DIC) images and phosphorescence images of the nanoparticle-labelled cells, demonstrating the possibility of detecting subcellular O_2 concentrations. The overall results indicated that CPdots possessed great potential for the quantification of oxygen in *in vitro* experiments dictated by their unique qualities, such as brightness, ratiometric emission, small size and, consequently, cellular uptake. Considering the advantage of these findings, in 2012, in Wang's lab,[157] PtOEP

was used to prepare a ratiometric FL probe, together with the O_2-insensitive dye coumarin 6 (C6) (λ_{ex} = 381 nm; λ_{em} = 510 nm), fabricated by the precipitation and encapsulation of the dyes within the matrix of PMMA nanoparticles, whose surface was functionalized with poly-L-lysine to facilitate cellular uptake and thus intracellular oxygen imaging visualization (Fig. 4a). The linear regression obtained by the Stern–Volmer plot, and the characterizations performed, allowed the authors to apply the nanoprobes in cellular cultures of the HepG2 human hepatocellular liver carcinoma cell line. CLSM images were

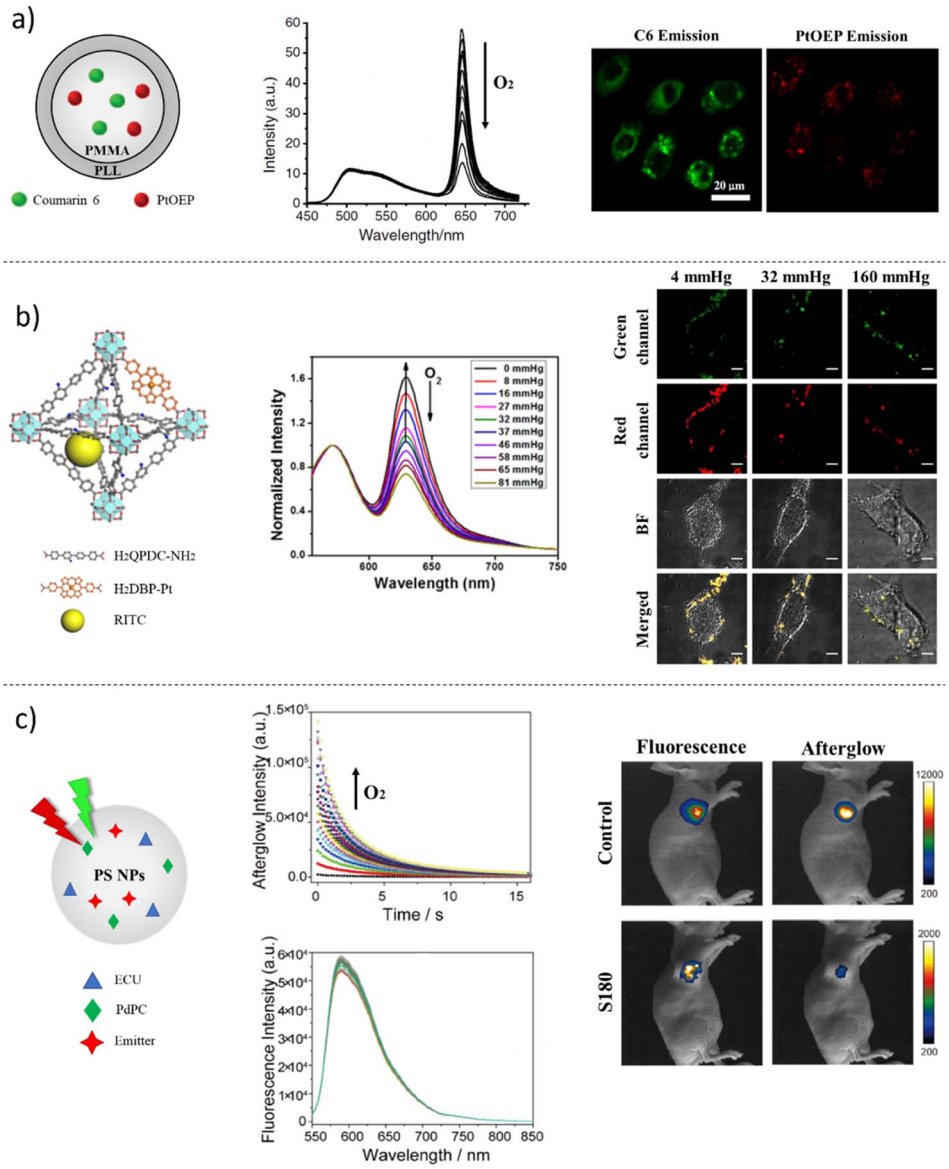

Fig. 4 Examples of O_2 sensing nano-platforms. (a) (Left) Schematic representation of the oxygen ratiometric PMMA-NPs; (middle): emission spectra of the sensor NPs at various concentrations of oxygen upon excitation at 381 nm excitation; (right): CLSM images of HepG2 cells loaded with the oxygen sensing NPs under normoxia conditions; the green fluorescence of C6 of ratiometric NPs was recorded using a 560 nm emission band-pass filter with a 405 nm excitation, while the red fluorescence of PtOEP using a 750 nm emission band-pass filter with a 543 nm excitation wavelength. Scale Bar: 20 μm. Reprinted with permission from Wang *et al.*, *Microchim Acta*, 2012, **178**, 147–152; Copyright © 2012, Springer-Verlag. (b) (Left): Schematic representation of R-UiO NMOF based on Pt(II)-porphyrin ligand as an O_2-sensitive probe and a rhodamine-B isothiocyanate ligand as an O_2-insensitive reference probe; (middle) emission spectra (λ_{ex} = 514 nm) of R-UiO in HBSS buffer under various oxygen partial pressures; (right): CLSM images of CT26 cells under hypoxia (4 mmHg), normoxia (32 mmHg), and aerated conditions (160 mmHg) after incubation with R-UiO-2. Scale bar: 5 μm. Reprinted with permission from Xu *et al.*, *J. Am. Chem. Soc.*, 2016, **138**, 2158–2161. Copyright © 2016, American Chemical Society. (c) (Left): Schematic illustration of the working principle of afterglow/fluorescence dual-emissive ratiometric O_2 probe; (middle): afterglow decay curves of AGNPs and fluorescence spectra of AGNPs in different oxygen concentrations; (right): fluorescence and afterglow images of mice with the subcutaneous implantation of AGNPs in the mouse bearing no tumor and of mice with the intratumor injection of AGNPs in the mouse bearing the tumor, with the corresponding fluorescence and afterglow intensity. Reprinted with permission from Wen *et al.*, *Anal. Chem.*, 2023, **95**, 4, 2478–2486. Copyright © 2023, American Chemical Society.

obtained after 12 hours of incubation of the NPs with cells in the culture medium. Assuming vesicular cellular uptake, the NPs were found to be localized in the intracellular space of HepG2 cells. By subjecting the cell cultures to hypoxia and normoxia conditions, Wang and collaborators were able to evaluate the goodness of the developed ratiometric FL O_2 analytical platform, confirming the potential of such a tool to sense intracellular oxygen concentrations.[157]

Based on the need to improve the existing O_2-sensing probes, Xu *et al.* developed a ratiometric metal–organic framework (MOF) for sensing intracellular oxygen (Fig. 4b).[158] MOFs are nanomaterials synthesized by bridging metal ions or clusters using organic ligands, which can be molecular sensing probes, thus preparing a final unit with a specific analytical scope.[159] For this reason, in recent years, researchers have explored MOFs as promising devices because of their intrinsic characteristics: first, encapsulated dyes and therapeutic drugs can diffuse easily from the core owing to the high porosity of the material; second, the encapsulation of sensing molecules can enhance the photostability and reduce the self-quenching phenomenon; lastly, the covalent bounds between the metal and organic linkers prevent unforeseen leaching.[160,161] Thus, exploiting the challenging properties of MOF, Xu and co-workers prepared a nanomaterial R-UiO-based having Pt-5,15-di(*p*-benzoato) porphyrin (H_2DBP-Pt) ($\lambda_{ex} = 570$ nm; $\lambda_{em} = 595$ nm) as bridging ligand, sensible to changes in O_2 concentration, and RBITC-conjugated quaterphenyldicarboxylate ($\lambda_{ex} = 570$ nm; $\lambda_{em} = 595$ nm), as reference fluorophore.[158] The authors recorded linear Stern–Volmer regression when the R-UiO was calibrated in the presence of different concentrations of O_2. The mouse colon carcinoma CT26 cell line was chosen as a cancer model, and Hank's balanced salt solution (HBSS) was used as a buffer medium for measuring O_2 intracellular levels. Through CLSM imaging, efficient cellular uptake was tracked and captured with image acquisitions after 2 hours of incubation of R-UiO MOFs with CT26 cells. The authors carried out the experiments using three O_2 concentrations: hypoxic (4 mmHg), normoxic (32 mmHg) and aerated (160 mmHg) conditions. The ratiometric calculations, obtained *via* the image analysis of the internalized R-UiO, corresponded to 5.1 ± 2.5, 27.3 ± 3.1, and 158 ± 11 mmHg; these data matched the theoretical O_2 values, demonstrating the accuracy of the proposed method. A step forward in imaging oxygen at tissue levels has been performed in a reported work of early 2023 published by Wen *et al.*, in which an afterglow/fluorescence dual-emissive ratiometric O_2 sensor was engineered (Fig. 4c).[162] In particular, the probe was based on a photochemical reaction-based afterglow system: the afterglow palladium(II) 1,4,8,11,15,18,22,25-octabutoxyphthalocyanine (PdPc) ($\lambda_{ex} = 730$ nm; $\lambda_{em} = 600$ nm) was the indicator dye sensitive to variations in O_2 concentration, while Nile Red (NR) ($\lambda_{ex} = 582$ nm; $\lambda_{em} = 600$ nm) represented the unquenchable O_2 dye. The reaction based on the ratiometric FL system occurred as follows: in the presence of O_2, the FL intensity of the afterglow gradually increased because of the formation of singlet oxygen species, whereas the reference NR maintained its FL peak unperturbed. The encapsulation of the fluorophores within polystyrene particles (AGNPs) using the swelling method facilitated dyes confinement, oxygen penetration, good solubility and viability.[162] The study by Wen and collaborators is significant because it is among the first studies on coupling afterglow/fluorescence sensing procedures for *in vitro* and *in vivo* experiments to explore the hypoxia environment in solid tumors. To this end, a mouse sarcoma S180 cell line was employed to test the cytotoxicity of the nanoparticles using a 3-(4,5-dimethylthiazol-2-yl)-2,5-diphenyltetrazolium bromide (MTT) assay. Finally, female athymic nude mice bearing mouse sarcoma cell-derived S180 and female athymic nude mice bearing no tumor were treated with AGNPs. After two weeks, the mice were imaged, showing a remarkable afterglow enhancement in mice with no tumor masses, while the afterglow signal was quite off in tumor bearing mice. In this way, the quantification of the O_2 concentration, using the ratio of the afterglow signal *versus* fluorescence intensity, in solid tumors in the area of injection of the AGNPs showed a 4.94-fold lower intensity compared to the ratio obtained in normal tissues. The study by Wen *et al.* proposed to the scientific community a stable and accurate ratiometric sensor for O_2 quantification *in vitro* and *in vivo*, but some efforts are still needed to improve the quantification of oxygen in deeper solid tumors.

2.3 Reactive oxygen species (ROS)

As mentioned previously, the most important ROS are hydrogen peroxide (H_2O_2), its reduction product hydroxyl radical ($^{\bullet}OH$), and superoxide anion radical ($O_2^{\bullet -}$).[70–72] In the complex landscape of TME, nanotechnologies play a fundamental role in ROS detection and monitoring. Consequently, in the last two decades, many efforts have been devoted to developing fluorescent probes for ROS sensing.[163,164] Two mechanisms exist by which non-fluorescent ROS-sensitive dyes are activated: H_2O_2 selective cleavage and oxidation. In 2008, Srikun and co-workers[165] published an internal charge transfer (ICT)-based approach to detect H_2O_2 in living cells using Peroxy Lucifer-1 (PL1) as a ratiometric fluorescent reporter. PL1 presents a 1,8-naphtalimide core structure with a 4-boronate-based carbamate protecting group that, once excited in the absence of H_2O_2, displays a blue emission peak ($\lambda_{ex} = 375$ nm; $\lambda_{em} = 475$ nm). In the presence of H_2O_2, PL1 loses the boronate-based carbamate protecting group by chemoselective cleavage, returning the green fluorescent aminonaphthalimide ($\lambda_{ex} = 435$ nm; $\lambda_{em} = 540$ nm). The biocompatible and ratiometric reactive dye PL1 was used to detect the endogenous concentration of H_2O_2 in RAW264.7 macrophages and HEK 293 T cells. Later on, Kim's group[166] prepared silica nanoparticles decorated with PL1. The aim was to develop a new scaffold as a promising tool for monitoring hydrogen peroxide. Currently, neither *in vitro* nor *in vivo* applications of PL1-SiO_2 particles have been reported in the literature. The most used probe for the detection of ROS and oxidative stress in cellular systems is the 2′,7′-dichlorofluorescein (DCF) dye. The enzymatic activity of esterases in the cytosol can convert the non-fluorescent diacetate form of 2′,7′-dichlorofluorescein (DCF-DA) in its hydrophilic form, generating a strong fluorescence response ($\lambda_{ex} = 488$ nm; $\lambda_{em} = 525$ nm) deriving, in a particular manner, from the oxidation

procured by H_2O_2 among other ROS. Kim and collaborators[167] developed a ratiometric nanoPEBBLE sensor to quantitatively estimate the H_2O_2 generation from stimulated RAW264.7 macrophages *in vitro*. After DCF-DA encapsulation into the ormosil nanoparticle matrix, the nanoprobe surface was functionalized with a reference dye, Alexa568 *N*-succinimidyl ester, and a membrane penetrating peptide, cysteine-terminated TAT peptide, which guided the delivery of the sensing PEBBLEs directly into the cytosol. In the lab of Kazakova,[168] the amphiphilic dye dihydrorhodamine 123 (DHR123) was employed as a sensing H_2O_2 unit in the fabrication of novel lactate microcapsule sensors. DHR123 is a non-emitting molecule, but in the presence of H_2O_2, it undergoes oxidation by generating the green emitting rhodamine 123 ($\lambda_{ex} = 488$ nm; $\lambda_{em} = 550$ nm). The novelty reported by Kazakova is involved in the concept of enzyme-assisted substrate sensing. In fact, the encapsulation of lactate oxidase (LOx, an enzyme that catalyses the transformation of L-lactate into pyruvate and H_2O_2)[169,170] coupled with the embedding of the amphiphilic ROS-sensitive fluorescent dye DHR123 onto the surface of calcium carbonate ($CaCO_3$) capsules, *via* the LbL deposition of oppositely charged polyelectrolytes, enabled to monitor H_2O_2 over time using an optical approach. The data reported in this study confirmed that the increased fluorescence of the DHR123 fluorophore ($\lambda_{ex} = 488$ nm; $\lambda_{em} = 550$ nm) is linearly correlated with the enzymatic activity of LOx and lactate concentration in the millimolar range. The results obtained here depicted the possibility of indirectly measuring lactate in the physio-pathological ranges and, by the further implementation of the following technique, paved the way for future monitoring of metabolites *in vitro* or *in vivo*.

Hydroxyl radicals ($^{\bullet}OH$) are recognized as the most dangerous free radicals among ROS because they come from H_2O_2 reduction in metal-catalysed Fenton chemistry, involving free iron (Fe^{2+}) ions. Liu *et al.*[171] developed a dye-doped-ratiometric fluorescent probe coupling the fluorescence response of coumarin-3-carboxylic acid (CCA), as indicator dye for $^{\bullet}OH$ detection and quantification, and 6-carboxy-X-rhodamine *N*-succinimidyl ester (ROX-SE), as a reference fluorophore (Fig. 5a). The blue-enhanced fluorescence emission of CCA is strictly linked to its reaction with $^{\bullet}OH$, which transforms CCA into 7-hydroxy coumarin 3-carboxylic acid product. The engineered ratiometric silica nanoparticles displayed a dual-emission fluorescent spectrum by employing a single excitation wavelength ($\lambda_{ex} = 395$ nm; $\lambda_{em} = 555$–620 nm). After the analytical method was validated, the authors monitored the nanoparticle uptake and detected $^{\bullet}OH$ levels in HeLa cells by live imaging. Importantly, cells incubated over time with 100 μM of $^{\bullet}OH$, in the presence of the sensing probe, displayed an increased blue fluorescent signal of CCA, whereas no changes in the red fluorescence of ROX were observed. Fluorescent sensing dyes, used as reporter and imaging agents, can be classified as FRET-based molecules when changes in the electronic interactions between a donor and an acceptor occur.[117] In analytical chemistry and live imaging applications, this concept is significantly being considered in the scientific literature because it permits the selective detection of target analytes of particular biological importance, such as in the case of ROS. The diselenide bond (Se–Se) represents a highly reactive linker with specific selectivity towards ROS because it is oxidized into the selenic acid. Deepagan *et al.*[172] successfully prepared an H_2O_2 on–off nanoprobe for an *in vitro* live imaging application (Fig. 5b). This nanosensor was based on the ability of gold nanoparticles to inhibit, in a distance-dependent manner, the fluorescence of surface-bound fluorescein isothiocyanate (FITC) dye *via* FRET in the absence of H_2O_2 ("off" state). When H_2O_2 concentration increased, the diselenide bond broke down selectively, releasing the free dye that could enhance its fluorescence ("on" state). The fluorescence characterization, performed in the presence of H_2O_2, demonstrated that the probe enhancement linearly depended on the concentration of hydrogen peroxide and allowed the authors to test the sensors in activated RAW264.7 macrophages to explore intracellular H_2O_2 changes over time. Other reactive groups, *i.e.* thiochetals,[173] phenylboronic acids and thioethers,[174] have been engaged as FRET-based sensors because they represent a nucleophilic anchor and a cleavable site for H_2O_2 species. An example of H_2O_2 sensitive FRET-based biosensor was developed by Feng's group.[175] The authors indirectly detected the glucose concentration produced by measuring the enzyme-catalysed H_2O_2 production carried out by glucose oxidase (GOx). For the fabrication of their sensing system, a self-assembly technique was employed using two functionalized lipophilic polymers: 4-carboxy-3-fluorophenylboronic acid (FPBA)-modified DSPE-PEG (DSPE-PEG-FPBA) and 7-hydroxycoumarin (HC)-conjugated DSPE-PEG (DSPE-PEG-HC). The addiction of Alizarin Red S (ARS) to the probe unit represents novelty. ARS is a non-fluorescent molecule, but its ability to create adducts with boronic acids makes possible the generation of a fluorescent signal. In this way, the detection approach developed by Feng *et al.* was based on the selective cleavage of ARS from FPBA caused by increased concentrations of H_2O_2. When no ARS was present in the polymeric micelles, the nanoprobe displayed a fluorescence peak in the blue region of the spectrum due to HC ($\lambda_{ex} = 405$ nm; $\lambda_{em} = 450$ nm). The subsequent addiction of ARS to the polymeric probe determined conjugation with FPBA and, consequently, the FRET phenomenon between the ARS-FPBA adduct and HC, which generated a new peak in the red region of the spectrum ($\lambda_{ex} = 405$ nm; $\lambda_{em} = 600$ nm). A ratiometric fluorescence response could then be recorded in the presence of H_2O_2. Under this condition, ARS was decoupled from the probe, resulting in a decrease in the emission peak at $\lambda_{em} = 600$ nm and an increase in fluorescence for the peak at $\lambda_{em} = 450$ nm. From a future perspective, the intrinsic potential of the multifunctional polymeric fluorescent probe proposed by Feng and collaborators can contribute to biochemical studies of the cell microenvironment.

QDs have also been successfully employed for H_2O_2 detection. For instance, Zhou *et al.*[176] described the preparation and application of TGA-capped Si–CdTe dual-emissive QDs for the selective monitoring of H_2O_2 in the intracellular space of HeLa cells. The coupling of Si-QSDs with CdTe QDs represented an innovation not only because of the addiction of a nanosized fluorescent unit but also because it skips the cytotoxicity

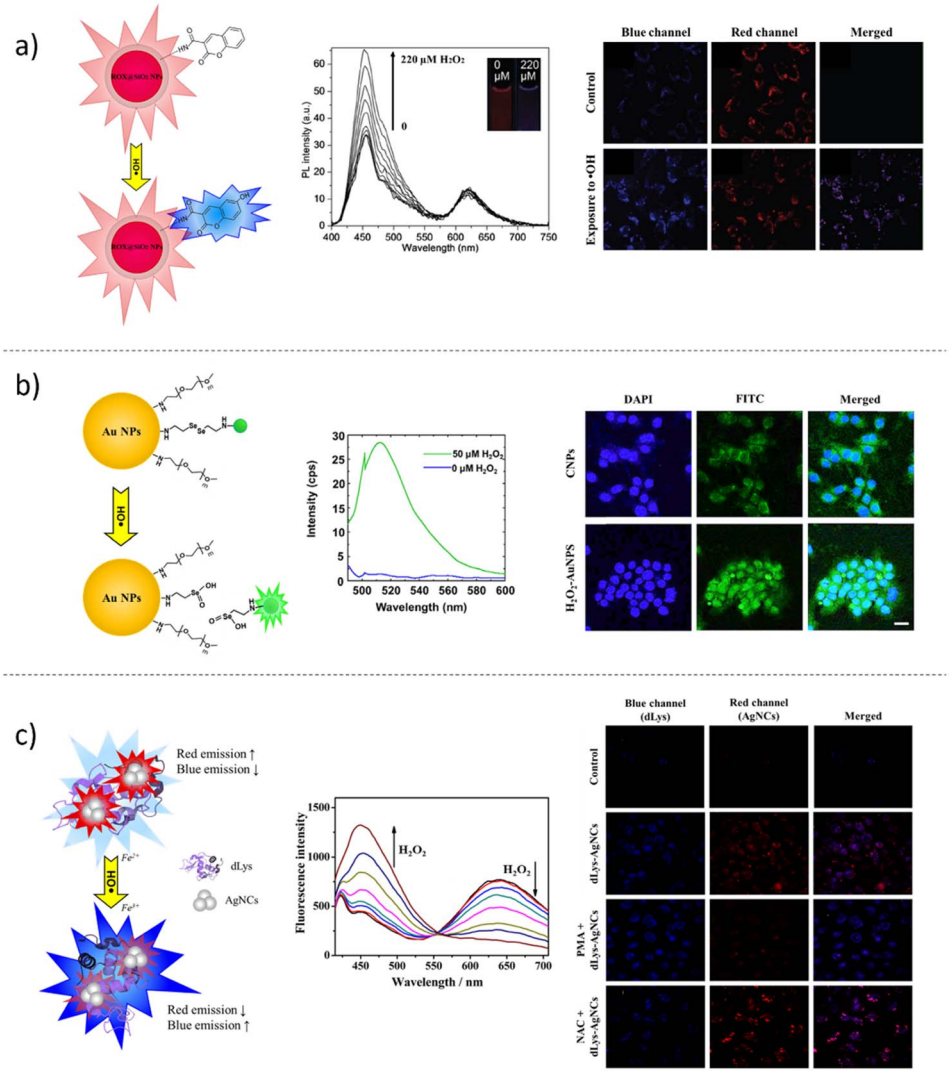

Fig. 5 Examples of ROS sensing nano-platforms. (a) (Left): Schematic illustration of the dual-emission probe synthesis procedure and the working principle for ratiometric fluorescence detection of •OH; (middle): fluorescence spectra of the ratiometric probe solution upon the exposure to different concentrations of •OH at various H_2O_2 concentrations; (right): confocal fluorescence images of HeLa cells after being incubated with the dual-emission probe in the absence and presence of •OH. The images were collected at 410–520 nm (blue channel) and 580–680 nm (red channel) upon excitation at 405 nm. Scale bar: 20 μm. Reprinted with permission of Royal Society of Chemistry, from Liu *et al.*, *Analyst*, 2016, **141**, 7, 2296–2302; permission conveyed through Copyright Clearance Center, Inc. (b) (Left): Schematic illustration of the H_2O_2-sensitive on-off H_2O_2-AuNPs; (middle): H_2O_2 responsive fluorescence spectra of H_2O_2 sensitive-AuNPs; (right): *in vitro* confocal microscopic images of activated RAW264.7 cells incubated with the CNPs and H_2O_2 –AuNPs for 3 hours at pH 7.4. Scale bar: 20 μm. Reprinted from Deepagan *et al.*, *Macromol. Res.*, 2018, **26**(7), 577–580. Copyright © 2018, The Polymer Society of Korea and Springer Science Business Media B.V., part of Springer Nature. (c) (Left): Schematic illustration of the fluorescent responding mechanism of dLys-AgNCs to Fenton Reagents; (middle): fluorescence spectra of the ratiometric NPs towards different H_2O_2 concentrations; (right): fluorescence confocal images of PC-3 cells alone (first raw), PC-3 cells treated with dLy-AgNC probe (second raw), PC-3 cells incubated with PMA (third raw) and NAC (forth raw) prior to treatment with dLys-AgNCs. Adopted from ref. Liu *et al.*, *Anal. Chem.*, 2016, **88**, 21, 10631–10638. Copyright © 2016 American Chemical Society.

problem using a silicon-based material, which has excellent solubility in water, great stability, and is easy to obtain. The FRET-sensing system reported by Zhou's group was based on the fluorescence intensity of blue Si-QDs (λ_{ex} = 370 nm; λ_{em} = 442 nm) and red CdTe QDs (λ_{ex} = 370 nm; λ_{em} = 562 nm). By gradually increasing the H_2O_2 concentration, the TGA-capping broke down; consequently, CdTe QDs fluorescence was reduced, whereas the Si-QDs emission became stronger in a linear relationship. By CLSM analyses of HeLa cells cultured with Si–CdTe QDs, the authors established a valid method to monitor H_2O_2 levels following nanoparticle uptake. Metallic nanoclusters (MNCs) are metal-centred nanoparticles stabilized by protective groups, usually biological molecules; for this reason, their employment as novel platforms for fluorescence sensing *in vitro* and *in vivo* has been increasing over the years. Among their properties, it is important to remark water-solubility and biocompatibility.[125,126] Liu *et al.* fabricated a dual-emissive fluorescent ratiometric probe for H_2O_2 and •OH

sensing based on lysozyme-capped silver nanoclusters (dLys-AgNCs) (Fig. 5c).[177] The fluorescent ratio, obtained between the quenching of the red peak at 640 nm and the enhancement at 450 nm due to ˙OH-induced oxidation of the tyrosine residue present in lysozyme, was linearly correlated with the H_2O_2 concentration. Live imaging experiments, performed using PC-3 cells after incubation with dLys-AgNCs, confirmed the ratiometric measurements. As a proof of concept, to the sensing system composed of PC-3 cells and dLy-AgNC probe, the authors added phorbol-12-myristate-13-acetate (PMA) and *N*-acetyl-cysteine (NAC), an ˙OH generation stimulator and a free radical scavenger, respectively. The fluorescence confocal analysis strengthened the ability of the dLys-AgNCs to detect and monitor *in vitro* changing levels in ˙OH.

2.4 Inorganic cations and anions (Ca^{2+}, Na^+, K^+, and Cl^-)

The leading phenomena that characterize the TME, such as acidosis, hypoxia and ROS generation, and drag with them also the dysregulation of ion fluxes, contributing to the enhancement of the cancer disorder and strong perturbations inside cells and in their surroundings. Involved in cancer processes, such as proliferation, invasion and metastasis, ions Ca^{2+}, Na^+, K^+ and Cl^- are the main players of cell–cell interactions and ECM digestions favouring the activation of specific signalling pathways.[178]

Calcium cations, Ca^{2+}, are involved in many cellular processes and signalling pathways; in particular, it is essential in muscle contraction, osteogenesis and neurotransmission.[179] Its concentration is kept constant in body fluids, which is around 100 nM in the cytosol and way higher in blood and interstitial fluids, around 2 mM.[180] These concentration differences should be maintained while designing intracellular or extracellular sensors. There are different FL probes for calcium cation imaging, and some of them are commercially available, such as fura, indo and fluo dyes. All these compounds contain multiple carboxylic functions that act as chelators for Ca^{2+}, in an "EDTA-like" motif, with different selectivities for other bivalent cations.[80,181] Si *et al.* reported the development of PEBBLE (Photonic Explorers for Bioanalysis with Biologically Localized Embedding) ratiometric nanosensors for Ca^{2+} imaging. The nanosensor was obtained by embedding the Ca^{2+} sensitive dye, Rhod-2, in polyacrylamide nanogels. To obtain a ratiometric probe, the Ca^{2+} insensitive dye Hilyte™ 647 was covalently conjugated to the nanogel surface. These PEBBLEs showed a K_d of 500–600 nM and were tested on PC-3 human prostate cancer cells for intracellular live imaging.[182] Lin *et al.* reported the synthesis and characterization of fluorescent Ca^{2+} nanosensors based on CDs. Fluorescent CDs were synthesized by the pyrolysis of citric acid, purified by applying dialysis and covered with a Ca^{2+} binding peptide (Fig. 6a). The peptide sequence was based on the EF-Hand domain of human calmodulin. The binding of Ca^{2+} cations to the nanosensors was able to quench the CD fluorescence, showing a sensitivity range in the micromolar range of concentration.[183] The toxicity of the nanosensors was evaluated on SH-SYS5 human neuroblastoma cells through MTT assay, proving the low toxicity of the nanoprobes. Schulz *et al.* reported the synthesis of Ca^{2+} cation nanosensors based on hybrid silica-dextran nanoparticles.[184] Silica nanoparticles were obtained by employing a modified Stöber method, doped with aminopropyl triethoxysilane (APTES) and covalently linked to RBITC. Fluo-4-modified aminodextran was used to form the outer shell around the silica. The conjugation was performed using disuccinimidyl carbonate as a linker between aminodextran and amino-modified nanoparticles. The ratiometric sensor showed a sensitivity range from 0 to 39.7 μM of Ca^{2+}, with a k_d of 780 nM, which can be suitable for intracellular Ca^{2+} imaging.

Sodium cations are the most abundant inorganic cations in the human body. They play a fundamental role in physiology, being involved in neurotransmission, muscle contraction and blood volume regulation.[179] The Na^+ concentration in bodily fluids can significantly vary. The typical concentration in blood is 135–150 mM, in the interstitial fluids is around 142 mM and in the cytosol is always maintained low at around 5–30 mM by the activity of ion pumps (such as Na^+/K^+ ATPase).[185] Fluorescent probes for Na^+ and K^+ imaging chemically differ from the Ca^{2+} ones. Instead of having polycarboxylic moieties, they have a typical ether crown, that can bind monovalent cations, and a fluorescent aromatic core.[80] One of the most used molecular probes for Na^+ cation imaging is SBFI (Sodium-Binding Benzofuran Isophthalate), which is 20-fold more selective for Na^+ compared to K^+, with a K_d of 20 mM, making SBFI useful for intracellular imaging. Sodium Green is another Na^+ sensitive fluorophore, with higher selectivity over potassium (41-fold more selective) and a lower K_d of 8.4 mM, which facilitates the detection of even smaller variations in sodium concentration. Other Na^+ sensitive fluorophores are CoroNa (with a K_d of 80 mM), ANa1 and ANa2.[185] Dietrich *et al.* reported the synthesis of Na^+ sensitive ratiometric nanosensors based on gold nanoparticles.[186] Sodium Green was used as the sensitive dye, while Texas red was used as the reference dye and both were embedded in the nanosensors by covering gold nanoparticles with layers of poly(vinylalcohol) and polyacetal. Nanosensors were incubated with CHO cells (Chinese hamster ovary cells), and Na^+ intracellular variations were monitored during the treatment with ionophores nigericin, gramicidin and monesin. Wang *et al.* reported the synthesis of ionophore-based fluorescent ratiometric nanosensors for Na^+ and K^+, by exploiting graphene quantum dots (G-QDs).[187] G-QDs were modified with propargyl bromide, and then a Cu^{2+}-catalysed Huisgen addition was used to coat the G-QDs with polyoxyethylene bis(azide). Sodium sensitive nanosensors were obtained by mixing PEG-GQDs with sodium ionophore X (NaX), sodium tetrakis-[3,5-bis(trifluoromethyl)-phenyl] borate (TFPB), bis(2-ethylhexyl) sebacate (DOS) and the oxazinoindolines (OX-R).[188] To obtain K^+ nanosensors, valinomycin was used instead of NaX. Both nanosensors displayed a sensitivity range between 0.1 mM and 1 M. One of the main limits in the use of this chromoionophore system is the interference of pH values in the readout of the sensors. However, Na^+ sensors were tested using HeLa cells to evaluate toxicity, showing good biocompatibility. To assess whether the nanosensors can detect alteration in the intracellular environment, HeLa cells were incubated with nanosensors

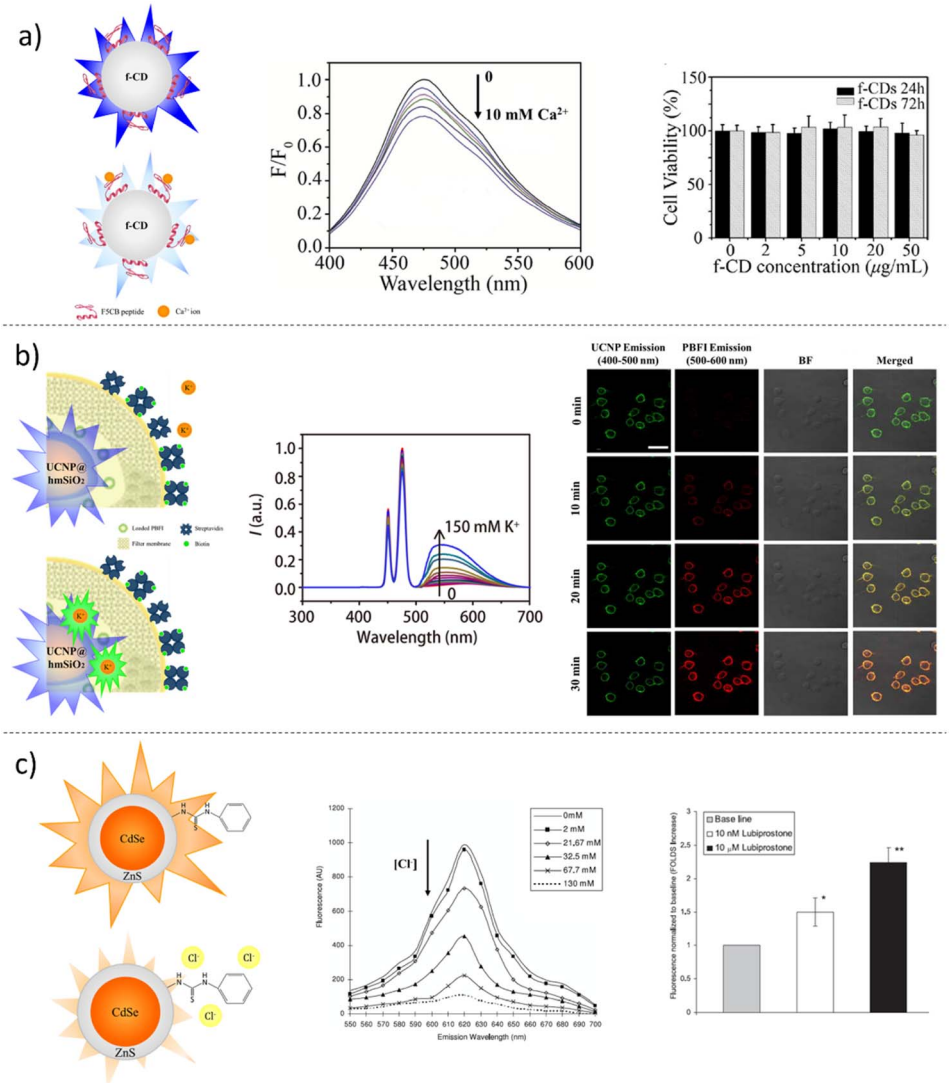

Fig. 6 Examples of ion ratiometric sensing platforms. (a) (Left): Schematic illustration of the peptide-functionalized carbon dots (f-CDs) that operate as Ca^{2+} nanosensors; (middle): fluorescence emission spectra of f-CDs at various concentrations of Ca^{2+} ($\lambda_{ex} = 350$ nm); the binding of calcium cations can quench the fluorescence emission of f-CDs; (right): cell viability assay on SH-SY5Y cells incubated at various concentrations of f-CDs for 24 and 72 hours. Reprinted with permission from Lin *et al.*, *Sens. Actuators, B*, 2018, **273**, 1654–1659. Copyright © 2018 Elsevier B.V. All rights reserved. (b) (Left): To the right: Schematic illustration of the K^+ nanosensors; the upconverting nanoparticles (UCNPs) are coated with PBFI-loaded silica and an outer shell of K^+ permeable film; (middle): fluorescence emission spectra of the nanosensors at various K^+ concentrations ($\lambda_{ex} = 808$ nm); (right): CLSM micrographs of HEK 293 cells labelled with K^+ nanosensors, showing fluorescence emission at 400–500 nm and 500–600 nm. The potassium cation efflux, after the treatment with 5 μM nigericin, 5 μM bumetanide, and 10 μM ouabain, is verified by the fluorescence enhancement of the PBFI. Reprinted with permission of ref. (Liu *et al.*, *Sci. Adv.*, **6**, eaax9757, 2020); figure licensed under a Creative Commons Attribution NonCommercial License 4.0 (CC BY-NC). (c) (Left): Schematic illustration of the Cl^- nanosensors; CdSe/ZnS quantum dots are capped with the chloride sensitive thiourea; (middle): fluorescence emission spectra of the Cl^- nanosensors at increasing concentration of chloride ($\lambda_{ex} = 425$ nm); (right): fluorescence emission of T84 cells incubated with the nanosensors and treated with Lubiprostone, showing the efflux of chloride anions from cells. Reproduced with permission from ref. Wang *et al.*, *Nanotechnology*, 2010, **21**, 055101. Copyright © 2010 IOP Publishing. All rights reserved.

and treated with gramicidin[189] and carbonyl cyanide 3-chlorophenylhydrazone (CCCP),[190] which act as ionophores on cell membranes. Fluctuation in fluorescence emission was monitored by applying CLSM, showing a decrease in intracellular Na^+ levels.

Potassium cations (K^+) are the most abundant cations in the intracellular compartment, with a mean concentration range of 140–150 mM, while in blood and extracellular fluids, it is lower at 3.5–5 mM.[191] K^+ cations play a crucial role in neurotransmission, muscle contraction, and insulin release and are also involved in pathological events, such as epilepsy, cardiac arrhythmia and cancer.[191] There are different fluorescent molecular probes for potassium cation imaging. The most widely employed probe is Potassium-Binding Benzofuran Isophthalate (PBFI), which suffers from poor selectivity between Na^+ and K^+, and an excitation peak in the far UV, with low

penetration capability and potentially harmful for living cells.[192] The Asante potassium green (APG or IPG) family of fluorophores is more selective compared to PBFI, with an excitation peak in visible light and with different K_d.[192] To overcome the limitation of PBFI as sensitive probes, Liu *et al.* reported the synthesis of K^+ nanosensors based on upconverting nanoparticles.[193] These nanoparticles display the ability to convert two or more photons into one photon with higher energy.[194] In this case, NaYF4:Yb/Tm nanoparticles were coated with silica, and then PBFI was embedded in an ion-selective polymer. This nanosensor design allowed for the excitation of PBFI with a near-infrared wavelength at 800 nm, increasing the tissue penetration capability. Moreover, the low selectivity of PBFI was improved by the ion-selective polymer. The shielded sensors displayed a sensitivity range between 2.8 μM and 150 mM of K^+. Nanosensors were tested on HEK 293 cell to assess their ability to monitor fluctuations in the extracellular environment using nigericin and bumetanide (the first as an ionophore and the latter as an inhibitor of the Na–K–Cl co-transporter).[195] Liu *et al.* reported the synthesis of K^+ nanosensors based on silica nanoparticles.[196] The silica nanoparticles were covered with an ion-selective polymer to trap the Asante potassium green 2 (APG-2) (Fig. 6b). This nanosensor showed a sensitivity range from 1.3 μM to 150 mM and was used in both *ex vivo* and *in vivo* models of murine epilepsy to monitor K^+ variations. Ruckh *et al.* reported the synthesis of a ratiometric K^+ nanosensor based on QDs.[197] The system comprised two QD species with non-overlapping emission spectra: a non-fluorescent chromoionophore and an ionophore. The protonation state of the chromoionophore affected its absorption spectra, with a consequent effect on the QD emission spectra. The final readout was derived from the ratio of the two QD species. The nanoparticles based on this system and embedded with a plasticizer displayed a sensitivity range of 2–120 mM. The nanoprobes were tested on HEK 293 cells to assess their ability to monitor K^+ fluctuations in the extracellular environment.

The chloride anion (Cl^-) is the most abundant anion in the human body and the most important in electrophysiological regulation. It plays a crucial role in neurotransmission and is also involved in pathological conditions, such as cystic fibrosis.[80] The chloride concentration inside cytosol can vary significantly in different cell lines, while in plasma and in interstitial, the concentration is maintained constant by kidney filtration at approximately 100 mM.[198] Most electrophysiological studies conducted on the Cl^- role in physio-pathological processes are performed with patch clamps, ion-selective electrodes and chloride radioisotope. However, different fluorescent molecular probes are commercially available for Cl^-, such as lucigenin (bis-*N*-methylacridinium nitrate), SPQ (6-methoxy-*N*-(3-sulfopropyl)quinolinium), MEQ (6-methoxy-*N*-ethylquinolinium), and BAC (10,10′ bis[3-carboxypropyl]-9,9′-biacridinium dinitrate). Ruedas-Rama *et al.* reported the synthesis of Cl^- nanosensors based on semiconductor QDs and lucigenin.[199] Hexadecylamine-capped CdSe/ZnS QDs were modified with 3-mercaptopropionic acid (MPA), and lucigenin was bound to nanoparticles by simple electrostatic interactions between the positively charged acridine and negatively charged MPA. The lucigenin fluorescence was quenched by Cl^- owing to a charge transfer mechanism. However, the QD–lucigenin conjugate showed increasing fluorescence emission in the QD spectrum, related to the competing action of FRET between QDs and lucigenin, and charge transfer between lucigenin and Cl^-. The calibration showed how the nanosensors could be used through FLIM or with the ratio between QD and lucigenin emissions. The system proved to be selective toward other anions and sensitive in the Cl^- concentration range of 0.5 mM to 50 mM. Wang *et al.* reported the synthesis of Cl^- nanosensors based on semiconductor quantum dots and a novel thiourea moiety. The 1-(2-mercapto-ethyl)-3-phenyl-thiourea was synthesized and used for the capping of CdSe/ZnS QDs (Fig. 6c).[200] The nanosensors displayed sensitivity in the range of Cl^- concentration from 2 mM to 130 mM. A comparison between the MEQ and nanosensors was performed using CF-PAC human epithelial cells. The two probes were embedded into liposomes and administered to CF-PAC cells treated with glibenclamide (as a chloride channel inhibitor). The nanosensors exhibited better sensitivity in monitoring intracellular Cl^- fluctuations, compared to MEQ by employing FLIM analyses.

2.5 Biomarkers

Macromolecules, such as nucleic acids, proteins, metabolites, isoenzymes and hormones, are well recognized as characteristic signatures of cancer onset and progression.[201] Biomarkers are molecules or substances that can indicate the presence or progression of a disease, and they are classified into three main categories in clinical practice: (i) diagnostic biomarkers, which are used for disease detection; (ii) prognostic biomarkers, which provide information about the likelihood of disease recurrence; and (iii) predictive biomarkers, which can help determine the patient's response to cancer treatment.[201] The most used methods to detect and quantify biomarkers are based on enzyme-linked immunosorbent assay (ELISA)[202] and polymerase-chain-reaction (PCR)-based protocols.[203] Although they are widely accepted as crucial procedures in cancer diagnosis and treatment, these technologies are not without limitations. One significant challenge is the slow reaction mechanism of detection, which can delay diagnosis and treatment initiation. Additionally, the exorbitant cost of reagents required for these techniques can result in high expenses for patients, limiting their accessibility and affordability.[202,203] Currently, there are only few published studies on ratiometric fluorescence-based nano-systems for cancer biomarkers.[204]

A strong correlation between extracellular pH acidification and the increased expression of tumor-related proteases is associated with the invasion and dissemination of cancer cells in other organs.[205,206] The quantification of matrix metalloproteases-2 (MMP-2) in the blood is still a great challenge because of the complexity of the biological fluid. In this context, Wang *et al.*[207] engineered an upconversion FRET-based biosensor to target MMP-2 particularly. The authors recorded a linear and proportional relationship between MMP-2 concentration and fluorescence recovery of the

sensing system in the range of 10–500 pg mL^{-1}. The validation of the bioanalytical sensors was carried out by collecting human plasma and whole blood samples. In the last 20 years, several efforts have been made to construct sensing platforms that can track the activity of proteases, exploiting their detection for the early diagnosis of cancer. An example is represented by the FL-gold nanoparticle activatable probes.[208–210] In 2008 and 2009, Lee and collaborators developed a NIR-FL gold nanoparticle that was selective for matrix metalloproteases-2 (MMP-2). Owing to its specificity, the developed probe facilitated the simple monitoring of the activities of MMP-2, both *in vitro*, using HepG2 cell line, and *in vivo*, adopting mice bearing SCC7 (squamous cell carcinoma) tumors.[211,212] In another work by Yin *et al.*,[213] an MMP-2 activatable probe was prepared by covalently coupling a near infrared dye (Cy5), a quencher (QSY21), a tumor targeting peptide (cyclic Arg-Gly-Asp) and a radionucleotide ^{125}I-labeled peptide substrate. The developed probe, which light-up upon proteolytic cleavage operated by active MMP-2, was employed for accurate detection *via* NIRF and single-photon emission computed tomography (SPECT) imaging techniques of the metastatic lymph nodes (MLNs) in mice bearing murine breast carcinoma cell line 4T1 before and during treatment with an MMP-2 inhibitor. The above-reported examples represent a fundamental application of highly selective and sensitive FL-based platforms and represent milestones in the field of ratiometric probes. In 2018, Ma *et al.* created an FL ratiometric probe to track matrix metallopeptidase-9 (MMP-9) activity and extracellular pH, both *in vitro* and *in vivo* (Fig. 7a).[214] The sensing platform was architected as follows: biocompatible-PEGylated iron oxide (Fe_3O_4) magnetic NPs were chosen as the sensor support material; the sensing units were represented by the pH-sensitive naphthalimide dye ANNA (λ_{ex} = 455 nm; λ_{em} = 510 nm) and labelled with a peptide substrate of MMP-9 (GGKGPLGLPG), and the reference dye Cy5.5 (λ_{ex} = 675 nm; λ_{em} = 695 nm) were covalently linked to PEGylated Fe_3O_4 NPs. The FRET-based mechanism determined the FL "off" state when the pH fluorophore ANNA was bound onto the surface of Fe_3O_4 NPs. The cleavage of the peptide substrate, operated by MMP-9, contributed to the FL enhancement of ANNA dye, which transitioned to the "on" state because of its protonation. Employing time-lapse CLSM, the ratiometric linear regression obtained by plotting $I_{ANNA}/I_{Cy5.5}$ allowed the authors to detect and quantify MMP-9, following the incubation of the ratiometric sensing probe in human colorectal cancer cell line LS180, which is known to overexpress MMP-9. To further validate the analytical platforms, the authors injected a ratiometric probe *via* the rat vein of tumor-bearing mice. The results showed that the nanoprobes were activated in the tumor site 4 hours post-injections, and the pH mapping and MMP-9 quantification, executed by image analysis, confirmed the possibility of real-time monitoring of multiple TME targets.

Another interesting target in clinical routine is telomerase, a transcriptase responsible for unlimited cancer proliferation.[215,216] For this reason, today, it is considered a diagnostic and prognostic biomarker. A QD-based ratiometric FL sensor, with an FRET mechanism, was developed by Ma *et al.* to specifically target intracellular telomerase activity (Fig. 7b).[217] The nanoprobe comprised a core–shell streptavidin-modified cadmium selenide/zinc sulphide core–shell (CdSe/ZnS) QD (QDs_{SA}) (λ_{ex} = 235 nm; λ_{em} = 600 nm), which was a functionalized with a telomerase primer (TP) and a signal switching sequence (SS), which was designed to form a hairpin filament complementary to telomerase. To obtain a sensing system, the SS was labelled at its 5′ end with cyanine 5 (Cy5) (λ_{ex} = 630 nm; λ_{em} = 665 nm) that acted as an FL acceptor. Thus, once assembled, the nanoprobe exhibited only the FL of Cy5 because of the FRET-phenomenon; in contrast, in the presence of telomerase, the TP was recognized and elongated by telomerase, hybridized with SS to form a double-strain and disassembled from the nanoprobe by providing the switch-on of QDs_{SA} and amplification of the FL signal, yielding a significant ratiometric FL change (F_{QDsSA}/F_{Cy5}). After optimization under the best sensing conditions, the nanoprobes were incubated with different interfering biomolecules, such as bovine serum albumin (BSA), immunoglobulin G (IgG), lysozyme, thrombin, trypsin, ATP, RNA, and Bst DNA polymerases. For none of these, the probe showed significant FL changes, thus presenting strong selectivity for telomerases. To map telomerase activity *in vitro*, the authors employed two types of cells: cervical carcinoma HeLa cells and human hepatocyte cells (L-O2). As expected, in cancerous HeLa cells, the green fluorescence of QDs_{SA} was visible, reflecting high telomerase activity, whereas the opposite result was obtained in healthy L-O2 cells. These results confirmed that intracellular telomerase can now be detected and monitored in a spatio-temporal manner owing to ratiometric FL platforms to be used, in the near future, as promising tools for diagnostic cancer screening and telomerase-targeted anticancer drugs.

With the advent/irruption of cancer liquid biopsy, the possibility of screening and detecting a high number of circulating tumor biomarkers, such as extracellular vesicles, proteins, nucleic acids, and microRNAs (miRNA), using simply a blood sample has become a reality.[218,219] A smart example of sensing colorectal cancer (CRC)-associated exosomal miRNA (miR-92a-3p), by developing ratiometric FL nanoparticles, was described in the work by Sun and collaborators (Fig. 7c).[220] The nanoprobe was composed of a hairpin DNA, labelled with sulfhydryl Atto-425 (λ_{ex} = 443 nm; λ_{em} = 482 nm) on the 5′ end and 3′ end, and conjugated to the surface of a fluorescent gold NPs (Au-NPs) (λ_{ex} = 320 nm; λ_{em} = 625 nm). In this way, the FL emissive peak of Atto-425 was quenched using a FRET mechanism by the FL of the Au-NPs. In contrast, in the presence of miR-92a-3p, Atto-425 was unbound from the surface of the Au-NPs, recovering its fluorescence. The detachment of Atto-425 was coordinated by the activity of a duplex-specific nuclease (DSN), which cleaved the DNA filament in a miR-92a-3p/DNA heteroduplex, keeping the RNA fragment intact. This process drove to signal amplification because the free miR-92a-3p could open another hairpin DNA, repeating the sensing cycle in this way.

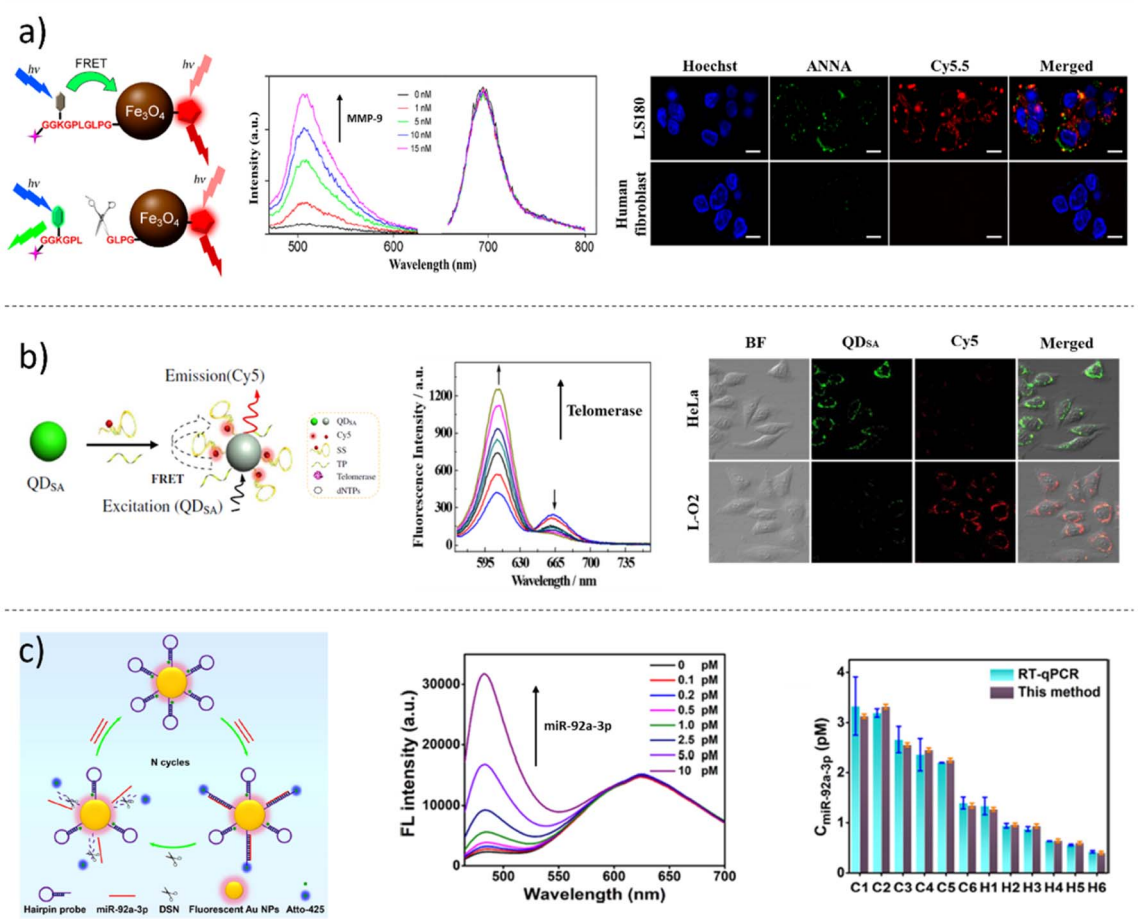

Fig. 7 Examples of biomarker sensing nano-platforms. (a) (Left): Schematic illustration of the working mechanism of Fe_3O_4 MMP-9 activity sensing NPs; (middle): fluorescence spectra recorded after the nanoprobes were incubated with different concentrations of activated MMP-9; (right): confocal microscopy images of LS180 cells (top row) and human fibroblast control cells (bottom row) obtained after incubation with the nanoprobe for 6 h and then imaged through different channels according to the dye emissions (cell nuclei were stained with Hoechst, and the scale bar corresponds to 10 μm). Reprinted with permission from Ma *et al.*, *J. Am. Chem. Soc.*, 2018, **140**, 1, 211–218. Copyright © 2018, American Chemical Society. (b) (left): The QDs_{SA}@DNA nanoprobe for monitoring of telomerase activity *in situ*; (middle): fluorescence emission spectra of the designed QDs_{SA}@DNA nanoprobe (100 nM) in response to telomerase extraction from different numbers of HeLa cells; (right): confocal fluorescence microscopy imaging of HeLa and L-O2 cells incubated with the QDs_{SA}@DNA nanoprobe for 4 h. The concentration of the added QDs_{SA}@DNA nanoprobe was 100 nM. Scale bar: 25 μm. Reprinted with permission from Ma *et al.*, *Anal. Bioanal. Chem.*, **414**, 1891–1898 (2022). Copyright © 2022, Springer-Verlag GmbH Germany, part of Springer Nature. (c) (left): Schematic of the ratiometric fluorescent detection of miR-92a-3p based on fluorescent Au-NP and DSN-assisted signal amplification; (middle): fluorescence spectra of the biosensor under different concentrations of miR-92a-3p; (right) comparison of the exosomal miR-92a-3p concentrations of CRC patients and healthy controls detected by RT-qPCR and this method (n = 3, mean ± s day). C1–C6 represents CRC patients; H1–H6 represents healthy controls. Reprinted with permission from Sun *et. al.*, *Bioconjugate Chem.*, 2022, **33**, 9, 1698–1706. Copyright © 2022, American Chemical Society.

The ratiometric calibration curve, carried out plotting the $I_{Atto425}/I_{Au\text{-}NPs}$, in a concentration range of 0.1–10 pM miR-92a-3p presented a linear regression fit of 0.995 and a limit of detection of 45 fM, thus improving the sensitivity in miRNA detection. After the lysis of exosomes, exosomal miR-92a-3p was extracted from the sera clinical samples of 3 CRC patients and 6 healthy controls. The results in the detection and quantification of miR-92a-3p extracted from patient and control samples using the ratiometric FL nanosensors agreed with those obtained by adopting real-time quantitative PCR (RT-qPCT). Thus, the biotechnological analytical platform can be considered a promising device and can be adopted as a potential tool in clinical diagnosis.

3. Hybrid materials/systems including fluorescent nano-microparticles for biomedical applications

Nowadays, monitoring the metabolic variations in TME *in toto* and simultaneously providing real-time detection at a single-cell scale are still challenging cues in cancer, tissue engineering and regenerative medicine.[221] The combination of diverse nanotechnologies has recently led to the development of integrated sensing devices that can reveal the spatio-temporal behaviour of cells using high-resolution and computational methods. Therefore, particle-reinforced biocomposites are

treated, in which the dispersed phase is represented by smart fluorescent nano- and microparticles for medical therapeutic and/or diagnostic purposes. The manipulation of parameters such as the volume ratios of the components and matrix type, including particle size and nature, geometry, orientation and distribution, offers wide design flexibility. Matrix materials of biomedical interest are represented by fibrous matrices based on biopolymers because they replicate the organization and biological behaviour of the extracellular matrix.[222] ECM-like fiber mats can be produced by electrospinning, which is a cost-effective method to fabricate fibers with diameters ranging from nanometers to microns.[223] Electrospun fibers exhibit many advantages, including tunable composition and size, tunable alignment, and the possibility of being loaded with drugs and stimuli-responsive nanomaterials to enable controlled and sustained release *via* physiological or physical stimuli.[224] Because of their size and surface features, nanofibers show a high surface-to-volume ratio and porosity, which favour the transport of small molecules as ions, making them a particularly attractive platform for the development of ultra-sensitive sensors. Thus, nano- and microparticle-based sensors can be dispersed in the polymer solution and entrapped by electrified jets within the lumen of the electrospun fibers, forming functional optical regions within the mats. The use of electrospinning to produce sensing matrices has been successfully reported by many groups.[225,226] For example, pH-sensing electrospun fiber scaffolds were produced by embedding pH sensors for the ratiometric measurement of local proton concentration, with high spatial resolution and in a fast and non-invasive manner.[227,228] The fluorescence changes in the functional regions were correlated with H^+ concentration during the spatio-temporal measurements of the extracellular acidity of pancreatic tumors and stromal co-cultures. Single-cell fermentation flux analysis, conducted *via* constraint-based inverse modelling, demonstrated that H^+ trafficking was strongly heterogeneous with just few cells showing high activity, and, therefore, responsible for a large fraction of the pH gradient in the cell culture (Fig. 8a).[228] Nano- and microparticles have also been incorporated in biopolymer-based hydrogels, which is a widely used class of materials in tissue engineering, ophthalmic, wound healing and drug delivery owing to their properties, such as biocompatibility and biodegradability.[229] Particle sensors can be easily dispersed within hydrogels, and because of their macromolecular polymer network structure and hydration, the mobility of small ions does not decrease significantly compared to their diffusion in aqueous solutions.[230,231] Among hydrogels, alginate is a naturally occurring biopolymer that has many applications owing to its biocompatibility, low cost, ease of gelation and optical transparency, which make it highly suitable even for microscopy applications. Very recently, alginate-based three-dimensional microgels were produced using an electrostatic droplet encapsulation method to embed FITC-RBITC SiO_2 pH sensors together with pancreatic tumor and/or stromal cells (Fig. 8b).[232] The method involved the use of high voltage to obtain droplets of an average diameter of around 200 μm, which were crosslinked in a solution of calcium chloride. Extracellular pH metabolic variations were monitored by applying 4D (x, y, z, t) live-cell imaging, showing that the pH was cell line-specific and time-dependent. In addition, differences in acidification were measured in 3D mono-against 3D cell co-cultures, suggesting the existence of cancer-stromal cell crosstalk resulting from metabolic cell reprogramming to a glycolytic phenotype.[233] The same droplet encapsulation method with alginate has also been used to incorporate pH-sensitive carbon nanoparticles for measuring pH during bacterial cultures. Ratiometric detection was assessed by calculating the ratio 550 nm/450 nm of fluorescence emissions that was plotted against the incubation time to obtain the growth rate of bacteria. The results showed that the emission ratio increased, and therefore the pH decreased over time, reflecting the growth of bacteria.[234] Luminescent amphiphilic carbon dots (CDs) nanoparticles were also embedded within an ascorbic acid derivative hydrogel to detect reactive oxygen species (ROS). ROS induced the oxidation of the ascorbic acid units with consequent collapse of the hydrogel, the aggregation of the CDs and therefore quenching of their luminescence, monitored under ultraviolet (UV) excitation. CD-hydrogel was applied as a sensing platform to detect *in vitro* the presence of ROS from HeLa cells, whether exposed to 5-fluorouracil (5-FU) or not. 5-FU is a chemotherapeutic known for generating intracellular ROS, leading to apoptosis of cancer cells.[235] Therefore, quenching of the CDs-hydrogel revealed the efficacy of the treatment, demonstrating the potential of the system for drug screening applications.[235] Recently, Delic *et al.* developed another fluorescent composite material from CDs. To preserve the intrinsic fluorescence in the dried solid state and in aqueous solution over a broad pH range (pH = 3–12), nanoparticles were dispersed and embedded throughout silica particles. Owing to hydrothermal treatment at low temperatures in the presence of urea and citric acid, a final fluorescent macroporous hollow structure, ideal for drug storage and delivery systems, was obtained.[236] Another ratiometric fluorescent microgel was produced by Li *et al.* from polyurethane (PU), a material widely used in medicine owing to its stability and biocompatibility. pH-sensing nanoparticles were loaded within the PU to obtain a final particle size distribution of around 75 μm and spherical morphology. Nanoparticles were synthesized by cross-linking denatured pH-sensitive bovine serum albumin proteins and pH-insensitive Nile Red as a reference and exhibited linear reversible fluorescence in response to pH ranging from 6 to 10. The system was used to study, through colorimetric maps, local extracellular pH during biomaterial degradation because this phenomenon could significantly affect the surrounding cells; for example, it could affect the balance between bone formation and resorption.[237] Fluorescent microparticles were also included in a polymer layer to create an integrated sensor for monitoring the oxygen gradients of hypoxic tumors. In particular, silica microparticles were first absorbed with oxygen-sensitive ($Ru(dpp)_3Cl_2$) and insensitive (Nile Blue chloride) fluorophores and then mixed with polydimethylsiloxane (PDMS). The mixture was then poured onto the pillars of a microfluidic device to recreate insulated oxygen conditions on the two sides of a monolayer of human breast cancer cell MCF7 and, therefore, hypoxic levels in the

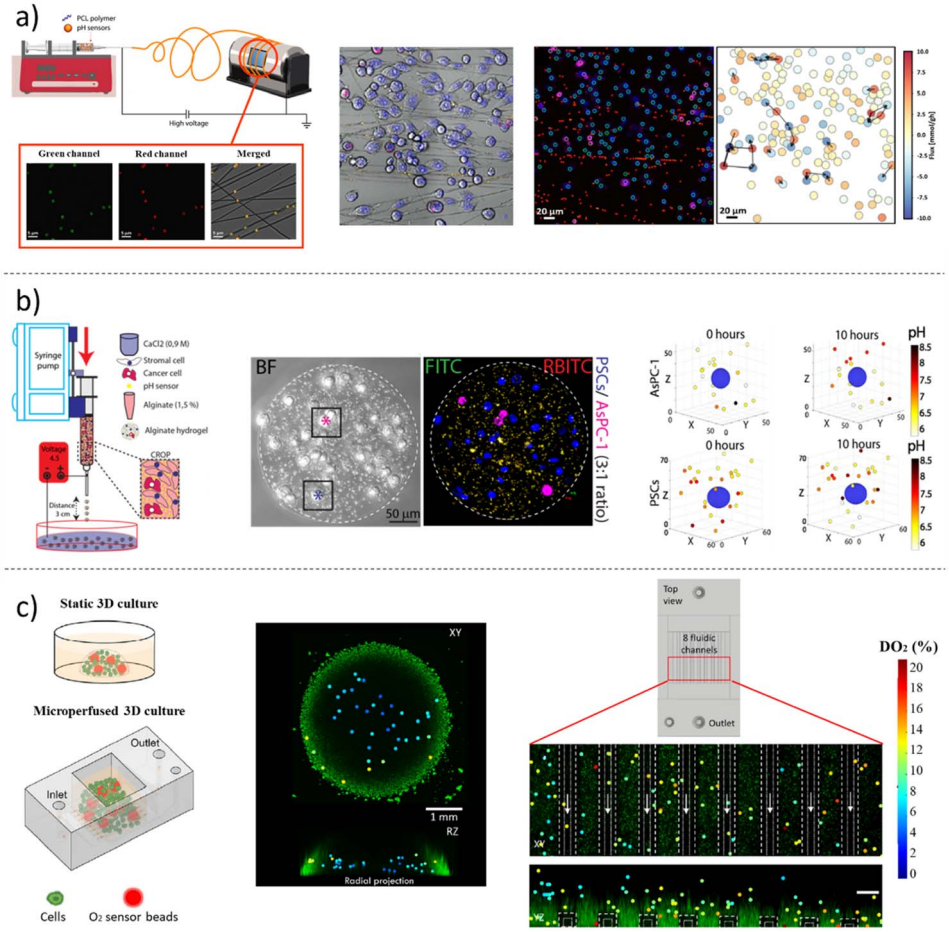

Fig. 8 Examples of hybrid materials/systems including fluorescent nano-microparticles for biomedical applications. (a) (left): Sketch showing the fabrication of electrospun polycaprolactone (PCL) fibers embedding ratiometric SiO_2-based microparticle sensors and representative CLSM micrographs showing PCL nanofibers embedding pH sensors (deposition time = 30 s). FITC (green channel), RBITC (red channel), and overlay with bright-field (BF, gray channel) are shown. Scale bar: 5 μm; (middle): representative CLSM image showing cells co-cultured on pH-sensing fibers and analyzed by CLSM time-lapse imaging (x, y, z, t; $t = 6$ h) (nuclei are shown in blue, and cell membranes are shown in magenta for tumor cells). (Right): Results of the segmentation show the detection of the single pH sensors (red circles), AsPC-1 cells (green circles), and CAF cells (yellow circles), corresponding to the reconstruction of the cell fluxes through physically constrained statistical inference, with a relative colormap. Scale bar: 20 μm. Reprinted with permission from Onesto *et al.*, *ACS Nano*, 2023, **17**, 3313–3323; figure licensed under CC-BY 4.0 https://creativecommons.org/licenses/by/4.0. (b) (Left): Schematic illustration of the microencapsulation system for the generation of 3D spherical hydrogel embedding pH sensors, tumor and stromal cells; (middle): maximum intensity projection of 3D time-lapse CLSM acquisitions of alginate hydrogel, including FITC/RBITC pH sensors (yellow), tumor cells (magenta) and stromal cells (blue). Bright-field (BF, grey). Scale bar: 50 μm. (Right): 3D scatter plots of the pH sensors around a selected tumor and cancer cells at times 0 and 10 h, with relative pH colourmaps. Reprinted with permission from Rizzo *et al.*, *Biosensors and Bioelectronics*, 2022, **212**, 114401; figure licensed under CC-BY 4.0 https://creativecommons.org/licenses/by/4.0. Copyright © 2022, The Authors. Published by Elsevier B.V. (c) (Left): The cell mixture is dispensed into the targeted 3D static culture, and 3D dynamic culture within a chip supporting microperfusion (perfusion pathway illustrated by arrows); (middle): CLSM PLIM imaging of the embedded oxygen sensor beads and subsequent conversion to the corresponding local oxygen concentration is shown as colour-coded concentrations overlaid with green fluorescence from calcein AM staining of metabolically active cells in lateral (XY) and radial (RZ) projections. HepG2 cells at 20×10^6 cells per mL embedded in a hydrogel of 7.5% w/v GelMA in a medium; (right): oxygenation in a 3D tissue model with an array of 8 perfused microfluidic channels (inner dimensions of 140×140 μm^2) and projected bottom view of sensor beads at all elevations overlaid on a projected confocal fluorescence micrograph of live-stained cells. Reproduced from Wesseler *et al.*, *Lab Chip*, 2022, **22**, 4167 with permission from the Royal Society of Chemistry.

monolayer. After 24 hours of cell culture, enhanced fluorescence of ruthenium was observed at the center of the pillar, which decreased radially. The ratiometric ruthenium by Nile Blue intensity was plotted against the radial distance; molecules and proteins regulated by hypoxia were immunostained and correlated with the oxygen gradient.[238] To monitor oxygen concentration within large 3D scaffolds, Wilson *et al.* reported the synthesis *via* organic-in-oil suspension of fluorescent hydrogel MPs containing palladium(II) meso(tetracarboxyphenyl)-porphine as an oxygen-sensitive fluorophore and Alexa Fluor 633 carboxylic acid tris(-triethylammonium) salt as reference fluorophore. MPs were encapsulated into a cellularized hydrogel scaffold, and oxygen gradients were measured *via* ratiometric imaging, showing that

the signals were robustly photostable and unaffected by hydrogel thicknesses of over 2 mm.[239] Another approach for monitoring oxygen gradients within a hydrogel environment, providing real-time information for ensuring efficient cell functions, involved the development of functional fluorescence-based nano-oxygen particles (FNOPs). In particular, pluronic F127-grafted polystyrene beads (PSBs) were linked with the commercially available oxygen-sensitive fluorescent molecule $Ru(dpp)_3Cl_2$ through hydrophobic interactions. FNOPs were applied to measure the oxygen concentration of RIN-m5F/HeLa cell lines in hydrogel spheres of 700–1000 μm in diameter generated by the electrospray technique for more than 5 days.[239] Oxygen concentration can also be probed using a confocal phosphorescence life-time microscope (PLIM).[98] Commercially available oxygen microsensor beads were mixed with the cell suspension in the presence or absence of gelatin methacryloyl (GelMA) as a photocrosslinkable hydrogel matrix, prior to seeding in static 2D, 3D cultures or in single or 8-channel array perfusion chips. To map and predict oxygen distributions for different cell densities, media and cultured cells, oxygen-dependent phosphorescence decay profiles of the microsensors can be converted through a calibration curve to oxygen concentration (Fig. 8c).[240] Finally, hybrid systems, including pH-fluorescent sensors, were developed by combining different technologies to probe 3D cell growth and tissue regeneration.[241] Capsules based on SNARF-1 were included in a 3D additive-manufactured scaffold with controlled geometry and porosity by providing a real-time detection of the acidification of human mesenchymal stromal cells. pH in the cell microenvironment showed a reduction after 7 days, which was more prominent at the edges of the 3D scaffolds, demonstrating the importance of considering the position of the sensors within a scaffold to detect smaller pH gradients that exist spatially around the cells.[242]

4. Challenges and future perspectives of ratiometric FL sensors in oncology

The feasibility and versatility of accurate and sensitive ratiometric FL sensing systems are explored in this review with a particular focus on their application for *in vitro* and *in vivo* spatiotemporal mapping of TME parameters, highlighting their potential for applications in cancer diagnostics and therapeutics. Among the many milestones achieved in this era, the possibility of adopting FL ratiometric sensors in clinical practice has become a reality and is now of great impact in surgery.[243] In fact, intraoperative FL-guided surgery can today discriminate a healthy tissue from a cancerous one, resulting in more accurate resection of the diseased area.[244–247] The main advantage coming from such fine surgical resection is the complete eradication of the tumor. Therefore, this procedure is strictly linked to the reduction of tumor metastasis circulation from a primary lesion to other organs. In addition to this, several other reports in the literature use ratiometric FL probes for mapping tumor's margins in biopsy tissues[248] or during surgery.[249] Frequently, surgery is accomplished by pharmacological therapies; therefore, another benefit that could be added to the clinical routine is the use of ratiometric FL sensing systems that can locally monitor drug release.[250] An example is represented by a recently developed ratiometric drug delivery system comprising a target-specific antibody for selective delivery to cancerous cells linked to a "drug-switchable dye" conjugate and a reference dye for the ratiometric fluorescence monitoring of drug release.[251–254] Using this system, the authors showed intensity-based monitoring of drug distribution and accumulation *in vitro* and *in vivo* as well as ratiometric measurements of drug release *in vitro*. Possible future developments could also include the fabrication and application of barcode ratiometric sensors for *in vitro*/*in vivo* multiplex spatiotemporal analysis of key metabolic TME parameters (*e.g.*, pH and oxygen) or metal ion concentrations (*e.g.*, calcium). Multiplexed non-invasive ratiometric sensing allows for the continuous and online recording of multiple cellular input signals influencing the physiological and pathological states of the body, thus improving our understanding of cell–cell interactions and cell response to therapies.

5. Conclusions

Fluorescence-based sensing and imaging have emerged as cutting-edge technologies for ratiometric fluorescence devices, providing accurate *in vitro* and *in vivo* detection and monitoring of TME parameters and related cancer biomarkers. The ability to capture cell–cell interactions and single-cell behaviour at different time points, qualitatively and quantitatively, allows for a deeper understanding of the complex world of cancer. This approach provides researchers and clinicians with precise and informative tools to fight against this widespread disease.

The design of smart ratiometric FL probes in the form of nano- and microparticles may seem straightforward at first glance. However, the working principles and effectiveness of a developed sensor platform depend on overcoming various obstacles that must be considered when imaging is the ultimate goal. Some of them are photostability, leaching, and autofluorescence generated by macromolecules in living organisms, as well as perturbations caused by operator, instrumental and environmental conditions, which can inevitably occur during the whole experiments. The strength of the ratiometric FL method depends on its self-calibration, achieved by employing an indicator signal and a reference signal, or two reversible signals, knocking down errors and enhancing accuracy and precision. In addition, the ongoing research and development of novel sensing probes spanning various options, including organic dyes, quantum dots, nanoclusters, and metal–organic frameworks, coupled with diverse synthetic methodologies, such as encapsulation and layer-by-layer (LbL) deposition of sensing units, the ability to customize particles with biocompatible molecules, and the ability to tune their size, shape, charge, and matrix support. These advancements have made ratiometric FL tools versatile platforms for sensing TME both *in vitro* and *in vivo*.

Today, the main players of the TME, including both cellular and non-cellular components, have been widely studied; even

though their leading functions in cancerogenesis and progression have been interpreted, the entire tumor pool still remains a constant-evolving topic. Phenomena such as acidosis, hypoxia, ROS generation, and ion fluxes variations are known to be strictly interconnected with each other, and all of them represent targets that are selectively hit by therapeutic protocols. Moreover, in the literature, it is possible to find many ratiometric FL tools for the detection of the intracellular and extracellular pH of cancer cells. More forces need to be engaged to develop ratiometric FL sensors for monitoring and real-time measurements of tumor hypoxia. However, intrinsically fluorescent nanomaterials, such as semiconductor quantum dots and metal nanoclusters, have emerged as promising candidates for the design of highly sensitive and photostable ratiometric FL systems. These nanomaterials have been successfully employed to monitor physio-pathological changes in pH, dissolved oxygen, ROS, and ion levels in tumor cells, and they have greatly assisted in the development of analytical platforms that are being used as point-of-care devices for the screening and targeting of diagnostic, prognostic, and predictive biomarkers. To overcome the challenge of mimicking the complex TME and capturing its metabolic dynamics in a spatiotemporal manner, ratiometric FL sensors have been successfully integrated into various biocompatible and easily handled polymer matrices to create 2D or 3D sensing platforms. This innovative approach offers the potential for high-resolution and reliable real-time measurements of cell metabolism during drug treatment, facilitating a more comprehensive understanding of TME and cell metabolic dynamics.

The future prospective is called "precision medicine" owing to the irruption of the nanotechnologies, which in turn are advancing daily toward more sophisticated and ultrasensitive platforms for boosting and gaining the finest and trustworthy quantification of the TME in its complexity. Owing to its related molecular biomarkers, cancer treatments will soon progress towards targeted therapies, the new revolutionary frontier.

Conflicts of interest

There are no conflicts to declare.

Acknowledgements

The authors acknowledge the funding from the European Research Council (ERC) under the European Union's Horizon 2020 research and innovation program ERC Starting Grant "INTERCELLMED" (contract number 759959), the European Union's Horizon 2020 research and innovation programme under grant agreement No. 953121 (FLAMIN-GO), the Associazione Italiana per la Ricerca contro il Cancro (AIRC) (MFAG-2019, contract number 22902), the "Tecnopolo per la medicina di precisione" (TecnoMed Puglia) – Regione Puglia: DGR n.2117 of 21/11/2018, CUP: B84I18000540002. The Italian Ministry of Research (MUR) under the complementary actions to the NRRP (PNC0000007) "Fit4MedRob-Fit for Medical Robotics" Grant (contract number CUP B53C22006960001) and the MUR NRRP "National Center for Gene Therapy and Drugs based on RNA Technology" (Project no. CN00000041 CN3 RNA). AC also acknowledges the Jain University, Bangalore (India) for its support through the provision of seed fund assistance.

References

1 P. Vineis and C. P. Wild, *Lancet*, 2014, **383**, 549–557.
2 American Cancer Society, *Cancer Facts & Figures*, 2022.
3 R. L. Siegel, K. D. Miller, N. S. Wagle, A. Jemal and C. A. Cancer, *J. Clin.*, 2023, **73**, 17–48.
4 K. R. Yabroff, X.-C. Wu, S. Negoita, J. Stevens, L. Coyle, J. Zhao, B. J. Mumphrey, A. Jemal and K. C. Ward, *JNCI, J. Natl. Cancer Inst.*, 2022, **114**, 907–909.
5 G. Schmidt, D. Dinter, M. F. Reiser and S. O. Schoenberg, *Dtsch. Ärztebl. Int.*, 2010, **107**, 383–389.
6 J. J. Vaquero and P. Kinahan, *Annu. Rev. Biomed. Eng.*, 2015, **17**, 385–414.
7 C. J. Garvey and R. Hanlon, *Br. Med. J.*, 2002, **324**, 1077–1080.
8 K. Christensen-Jeffries, O. Couture, P. A. Dayton, Y. C. Eldar, K. Hynynen, F. Kiessling, M. O'Reilly, G. F. Pinton, G. Schmitz, M. X. Tang, M. Tanter and R. J. G. van Sloun, *Ultrasound Med. Biol.*, 2020, **46**, 865–891.
9 T.-J. Yoon, *World J. Gastrointest. Endosc.*, 2013, **5**, 534.
10 J. A. Joyce, *Cancer Cell*, 2005, **7**, 513–520.
11 P. A. Kenny, G. Y. Lee and M. J. Bissell, *Front. Biosci.*, 2007, **12**, 3468–3474.
12 N. E. Sounni and A. Noel, *Clin. Chem.*, 2013, **59**, 85–93.
13 C. Roma-Rodrigues, R. Mendes, P. Baptista and A. Fernandes, *Int. J. Mol. Sci.*, 2019, **20**, 840.
14 Y. Xiao and D. Yu, *Pharmacol. Ther.*, 2021, **221**, 107753.
15 L. Bejarano, M. J. C. Jordão and J. A. Joyce, *Cancer Discovery*, 2021, **11**, 933–959.
16 C. Belli, G. Antonarelli, M. Repetto, M. Boscolo Bielo, E. Crimini and G. Curigliano, *Cancers*, 2022, **14**, 4278.
17 E. Henke, R. Nandigama and S. Ergün, *Front. Mol. Biosci.*, 2020, **6**, 1–24.
18 O. Tredan, C. M. Galmarini, K. Patel and I. F. Tannock, *JNCI, J. Natl. Cancer Inst.*, 2007, **99**, 1441–1454.
19 Y. Xu, X. Hu, S. Kundu, A. Nag, N. Afsarimanesh, S. Sapra, S. C. Mukhopadhya and T. Han, *Sensors*, 2019, **19**, 2908.
20 R. Jenjob, T. Phakkeeree and D. Crespy, *Biomater. Sci.*, 2020, **8**, 2756–2770.
21 W. A. Flavahan, E. Gaskell and B. E. Bernstein, *Science*, 2017, **357**, 1–20.
22 K. Pruitt, in *Progress in Molecular Biology and Translational Science*, Elsevier Inc., 1st edn, 2016, vol. 144, pp. 3–47.
23 I. P. Pogribny, *Exp. Oncol.*, 2010, **32**, 132–136.
24 S. T. Boyle, M. Zahied Johan and M. S. Samuel, *J. Cell Sci.*, 2021, **133**, 1–9.
25 I. Elia and M. C. Haigis, *Nat. Metab.*, 2021, **3**, 21–32.
26 J. Winkler, A. Abisoye-Ogunniyan, K. J. Metcalf and Z. Werb, *Nat. Commun.*, 2020, **11**, 1–19.
27 M. Wang, J. Zhao, L. Zhang, F. Wei, Y. Lian, Y. Wu, Z. Gong, S. Zhang, J. Zhou, K. Cao, X. Li, W. Xiong, G. Li, Z. Zeng and C. Guo, *J. Cancer*, 2017, **8**, 761–773.

28 H. F. Dvorak, V. M. Weaver, T. D. Tlsty and G. Bergers, *J. Surg. Oncol.*, 2011, **103**, 468–474.
29 H. A. Goubran, R. R. Kotb, J. Stakiw, M. E. Emara and T. Burnouf, *Cancer Growth Metastasis*, 2014, **7**, CGM.S11285.
30 S. Balani, L. V. Nguyen and C. J. Eaves, *Nat. Commun.*, 2017, **8**, 1–10.
31 D. P. Tabassum and K. Polyak, *Nat. Rev. Cancer*, 2015, **15**, 473–483.
32 T. D. Tlsty and P. W. Hein, *Curr. Opin. Genet. Dev.*, 2001, **11**, 54–59.
33 O. De Wever and M. Mareel, *J. Pathol.*, 2003, **200**, 429–447.
34 X. Mao, J. Xu, W. Wang, C. Liang, J. Hua, J. Liu, B. Zhang, Q. Meng, X. Yu and S. Shi, *Mol. Cancer*, 2021, **20**, 1–30.
35 Y. An, F. Liu, Y. Chen and Q. Yang, *J. Cell. Mol. Med.*, 2020, **24**, 13–24.
36 B. Sun, *Cell Rep. Phys. Sci.*, 2021, **2**, 100515.
37 S. Xu, H. Xu, W. Wang, S. Li, H. Li, T. Li, W. Zhang, X. Yu and L. Liu, *J. Transl. Med.*, 2019, **17**, 1–22.
38 S. Spada, A. Tocci, F. Di Modugno and P. Nisticò, *J. Exp. Clin. Cancer Res.*, 2021, **40**, 1–14.
39 M. Liu, C. Tolg and E. Turley, *Front. Immunol.*, 2019, **10**, 1–9.
40 X. Zhang, D. Nie and S. Chakrabarty, *Front. Biosci.*, 2010, **15**, 151–165.
41 V. Poltavets, M. Kochetkova, S. M. Pitson and M. S. Samuel, *Front. Oncol.*, 2018, **8**, 1–19.
42 G. Maguire, *Neural Regener. Res.*, 2018, **13**, 1185–1186.
43 F. D. S. E. Melo, L. Vermeulen, E. Fessler and J. P. Medema, *EMBO Rep.*, 2013, **14**, 686–695.
44 R. Baghban, L. Roshangar, R. Jahanban-Esfahlan, K. Seidi, A. Ebrahimi-Kalan, M. Jaymand, S. Kolahian, T. Javaheri and P. Zare, *Cell Commun. Signaling*, 2020, **18**, 1–19.
45 R. G. Jones and C. B. Thompson, *Genes Dev.*, 2009, **23**, 537–548.
46 K. Fernald and M. Kurokawa, *Trends Cell Biol.*, 2013, **23**, 620–633.
47 F. Spill, D. S. Reynolds, R. D. Kamm and M. H. Zaman, *Curr. Opin. Biotechnol.*, 2016, **40**, 41–48.
48 M. J. Oudin and V. M. Weaver, *Cold Spring Harbor Symp. Quant. Biol.*, 2016, **81**, 189–205.
49 T. R. Cox, *Nat. Rev. Cancer*, 2021, **21**, 217–238.
50 D. Ribatti and F. Pezzella, *Cells*, 2021, **10**, 1–13.
51 A. G. Clark and D. M. Vignjevic, *Curr. Opin. Cell Biol.*, 2015, **36**, 13–22.
52 M. Castaneda, P. den Hollander, N. A. Kuburich, J. M. Rosen and S. A. Mani, *Semin. Cancer Biol.*, 2022, **87**, 17–31.
53 H. S. Chae and S. T. Hong, *Int. J. Mol. Sci.*, 2023, **24**, 12–41.
54 S. Aki, R. Nakahara, K. Maeda and T. Osawa, *BBA, Biochim. Biophys. Acta, Gen. Subj.*, 2023, **1867**, 130330.
55 R. J. DeBerardinis and N. S. Chandel, *Nat. Metab.*, 2020, **2**, 127–129.
56 O. Warburg, *Science*, 1956, **123**, 309–314.
57 S. Y. Lunt and M. G. Vander Heiden, *Annu. Rev. Cell Dev. Biol.*, 2011, **27**, 441–464.
58 E. Pérez-Herrero and A. Fernández-Medarde, *Acta Pharm. Sin. B*, 2021, **11**, 2243–2264.
59 E. Boedtkjer and S. F. Pedersen, *Annu. Rev. Physiol.*, 2020, **82**, 103–126.
60 M. R. Greco, L. Moro, S. Forciniti, K. Alfarouk, S. Cannone, R. A. Cardone and S. J. Reshkin, *Int. J. Mol. Sci.*, 2021, **22**, 1–13.
61 D. E. Korenchan and R. R. Flavell, *Cancers*, 2019, **11**, 1–17.
62 B. A. Webb, M. Chimenti, M. P. Jacobson and D. L. Barber, *Nat. Rev. Cancer*, 2011, **11**, 671–677.
63 P. Swietach, *Cancer Metastasis Rev.*, 2019, **38**, 5–15.
64 V. Huber, A. De Milito, S. Harguindey, S. J. Reshkin, M. L. Wahl, C. Rauch, A. Chiesi, J. Pouysségur, R. A. Gatenby, L. Rivoltini and S. Fais, *J. Transl. Med.*, 2010, **8**, 57–60.
65 K. A. White, B. K. Grillo-Hill and D. L. Barber, *J. Cell Sci.*, 2017, **130**, 663–669.
66 F. Parades, H. C. Williams and A. San Martin, *Cancer Lett.*, 2021, **502**, 133–142.
67 A. J. Majmundar, W. J. Wong and M. C. Simon, *Mol. Cell*, 2010, **40**, 294–309.
68 B. Muz, P. de la Puente, F. Azab and A. K. Azab, *Hypoxia*, 2015, **3**, 83–92.
69 R. Missiaen, N. P. Lesner and M. C. Simon, *EMBO J.*, 2023, e112067.
70 M. Assi, *Am. J. Physiol.: Regul., Integr. Comp. Physiol.*, 2017, **313**, R646–R653.
71 V. Aggarwal, H. S. Tuli, A. Varol, F. Thakral, M. B. Yerer, K. Sak, M. Varol, A. Jain, M. A. Khan and G. Sethi, *Biomolecules*, 2019, **9**, 79–86.
72 A. Kirtonia, G. Sethi and M. Garg, *Cell. Mol. Life Sci.*, 2020, **77**, 4459–4483.
73 F. Colella, G. Scillitani and C. L. Pierri, *Toxicology*, 2021, **447**, 152612.
74 B. Zhang, C. Pan, C. Feng, C. Yan, Y. Yu, Z. Chen, C. Guo and X. Wang, *Redox Rep.*, 2022, **27**, 45–52.
75 B. Chance, H. Sies and A. Boveris, *Physiol. Rev.*, 1979, **59**, 527–605.
76 H. Sies, *Redox Biol.*, 2017, **11**, 613–619.
77 H. Sies and D. P. Jones, *Nat. Rev. Mol. Cell Biol.*, 2020, **21**, 363–383.
78 C. Gorrini, I. S. Harris and T. W. Mak, *Nat. Rev. Drug Discovery*, 2013, **12**, 931–947.
79 J. Zheng, *Oncol. Lett.*, 2012, **4**, 1151–1157.
80 J. Krämer, R. Kang, L. M. Grimm, L. De Cola, P. Picchetti and F. Biedermann, *Chem. Rev.*, 2022, **122**, 3459–3636.
81 N. Prevarskaya, R. Skryma and Y. Shuba, *Trends Mol. Med.*, 2010, **16**, 107–121.
82 A. Becchetti, L. Munaron and A. Arcangeli, *Front. Physiol.*, 2013, **4**, 1–3.
83 E. Bates, *Annu. Rev. Cell Dev. Biol.*, 2015, **31**, 231–247.
84 M. Futai, T. Oka, G. H. Sun-Wada, Y. Moriyama, H. Kanazawa and Y. Wada, *J. Exp. Biol.*, 2000, **203**, 107–116.
85 M. Levin, *BioEssays*, 2012, **34**, 205–217.
86 D. S. Adams and M. Levin, *Cell Tissue Res.*, 2013, **352**, 1–50.
87 C. A. Jones and L. A. Hazlehurst, *Biomedicines*, 2021, **9**, 1200.
88 T. A. Stewart, K. T. D. S. Yapa and G. R. Monteith, *Biochim. Biophys. Acta, Biomembr.*, 2015, **1848**, 2502–2511.

89 B. Chovancova, V. Liskova, P. Babula and O. Krizanova, *Biomolecules*, 2020, **10**, 1–10.
90 T. K. Leslie, A. D. James, F. Zaccagna, J. T. Grist, S. Deen, A. Kennerley, F. Riemer, J. D. Kaggie, F. A. Gallagher, F. J. Gilbert and W. J. Brackenbury, *Biochim. Biophys. Acta, Rev. Cancer*, 2019, **1872**, 1–38.
91 X. Huang and L. Y. Jan, *J. Cell Biol.*, 2014, **206**, 151–162.
92 T. Mijatovic, F. Dufrasne and R. Kiss, *Pharm. Pat. Anal.*, 2012, **1**, 91–106.
93 H. J. Kim, P. C.-W. Lee and J. H. Hong, *Cancers*, 2022, **14**, 856.
94 J. Shi, P. W. Kantoff, R. Wooster and O. C. Farokhzad, *Nat. Rev. Cancer*, 2017, **17**, 20–37.
95 E. S. Kawasaki and A. Player, *Nanomedicine*, 2005, **1**, 101–109.
96 M. J. Sanderson, I. Smith, I. Parker and M. D. Bootman, *Cold Spring Harb. Protoc.*, 2014, **10**, 1–36.
97 R. Datta, T. M. Heaster, J. T. Sharick, A. A. Gillette and M. C. Skala, *J. Biomed. Opt.*, 2020, **25**, 1.
98 P. S. Chelushkin and S. P. Tunik, in *Springer Series in Chemical Physics*, Springer International Publishing, 2019, vol. 119, pp. 109–128.
99 P. Liu, R. Zhao, H. Li, T. Zhu, Y. Li, H. Wang and X.-D. ZHang, *Nano Res.*, 2023, **16**, 692–714.
100 M. Anderson, A. Moshnikova, D. M. Engelman, Y. K. Reshetnyak and O. A. Andreev, *Proc. Natl. Acad. Sci. U. S. A.*, 2016, **113**, 8177–8181.
101 X. Zheng, H. Tang, C. Xie, J. Zhang, W. Wu and X. Jiang, *Angew. Chem., Int. Ed.*, 2015, **54**, 8094–8099.
102 X. Zheng, X. Wang, H. Mao, W. Wu, B. Liu and X. Jiang, *Nat. Commun.*, 2015, **6**, 5834.
103 X. Zheng, H. Mao, D. Huo, W. Wu, B. Liu and X. Jiang, *Nat. Biomed. Eng.*, 2017, **1**, 1–9.
104 S. C. A. Yeh, J. Hou, J. W. Wu, S. Yu, Y. Zhang, K. D. Belfield, F. D. Camargo and C. P. Lin, *Nat. Commun.*, 2022, **13**, 1–13.
105 G. Rong, E. E. Tuttle, A. N. Reilly and H. A. Clark, *Annu. Rev. Anal. Chem.*, 2019, **12**, 109–128.
106 G. Rong, S. R. Corrie and H. A. Clark, *ACS Sens.*, 2017, **2**, 327–338.
107 S. J. Kim, S. J. Choi, J. S. Jang, H. J. Cho and I. D. Kim, *Acc. Chem. Res.*, 2017, **50**, 1587–1596.
108 A. Turner, I. Karube and G. S. Wilson, *Biosensors: Fundamentals and Applications*, Oxford University Press, New York, Oxford, 1st edn, 1987.
109 S. E. Eklund, D. Taylor, E. Kozlov, A. Prokop and D. E. Cliffel, *Anal. Chem.*, 2004, **76**, 519–527.
110 M. A. Boyd, A. M. Davis, N. R. Chambers, P. Tran, A. Prindle and N. P. Kamat, *Cell. Mol. Bioeng.*, 2021, **14**, 459–469.
111 X. Huang, X. Teng, D. Chen, F. Tang and J. He, *Biomaterials*, 2010, **31**, 438–448.
112 T. S. Atabaev, G. Urmanova and N. H. Hong, *Nano LIFE*, 2014, **04**, 1441003.
113 P. Anger, P. Bharadwaj and L. Novotny, *Phys. Rev. Lett.*, 2006, **96**, 3–6.
114 X. Pei, Y. Pan, L. Zhang and Y. Lv, *Appl. Spectrosc. Rev.*, 2020, 1–22.
115 X. Huang, J. Song, B. C. Yung, X. Huang, Y. Xiong and X. Chen, *Chem. Soc. Rev.*, 2018, **47**, 2873–2920.
116 H. J. Park, D. J. Shin and J. Yu, *J. Chem. Educ.*, 2021, **98**, 703–709.
117 L. Wu, C. Huang, B. P. Emery, A. C. Sedgwick, S. D. Bull, X. P. He, H. Tian, J. Yoon, J. L. Sessler and T. D. James, *Chem. Soc. Rev.*, 2020, **49**, 5110–5139.
118 S. Kargozar, S. J. Hoseini, P. B. Milan, S. Hooshmand, H. Kim and M. Mozafari, *Biotechnol. J.*, 2020, **15**, 2000117.
119 W. A. A. Mohamed, H. Abd El-Gawad, S. Mekkey, H. Galal, H. Handal, H. Mousa and A. Labib, *Nanotechnol. Rev.*, 2021, **10**, 1926–1940.
120 U. Resch-Genger, M. Grabolle, S. Cavaliere-Jaricot, R. Nitschke and T. Nann, *Nat. Methods*, 2008, **5**, 763–775.
121 A. Valizadeh, H. Mikaeili, M. Samiei, S. M. Farkhani, N. Zarghami, M. Kouhi, A. Akbarzadeh and S. Davaran, *Nanoscale Res. Lett.*, 2012, **7**, 19–21.
122 S. Pandey and D. Bodas, *Adv. Colloid Interface Sci.*, 2020, **278**, 102137.
123 H. D. Duong and J. Il Rhee, *Sensors*, 2019, **19**, 4977.
124 M. Hu, J. Tian, H. T. Lu, L. X. Weng and L. H. Wang, *Talanta*, 2010, **82**, 997–1002.
125 F. Wen, Y. Dong, L. Feng, S. Wang, S. Zhang and X. Zhang, *Anal. Chem.*, 2011, **83**, 1193–1196.
126 R. Shen, P. Liu, Y. Zhang, Z. Yu, X. Chen, L. Zhou, B. Nie, A. Zaczek, J. Chen and J. Liu, *Anal. Chem.*, 2018, **90**, 4478–4484.
127 J. Hou, W. X. Ren, K. Li, J. Seo, A. Sharma, X.-Q. Yu and J. S. Kim, *Chem. Soc. Rev.*, 2017, **46**, 2076–2090.
128 D. E. Johnson, P. Ostrowski, V. Jaumouillé and S. Grinstein, *J. Cell Biol.*, 2016, **212**, 677–692.
129 A. Kurkdjian and J. Guern, *Annu. Rev. Plant Physiol. Plant Mol. Biol.*, 1989, **40**, 271–303.
130 M. Flinck, S. H. Kramer and S. F. Pedersen, *Acta Physiol.*, 2018, **223**, 1–17.
131 J. Han and K. Burgess, *Chem. Rev.*, 2010, **110**, 2709–2728.
132 A. Steinegger, O. S. Wolfbeis and S. M. Borisov, *Chem. Rev.*, 2020, **120**, 12357–12489.
133 L. L. del Mercato, P. Rivera-gil, A. Z. Abbasi, M. Ochs, C. Ganas, I. Zins, C. Sonnichsen and W. J. Parak, *Nanoscale*, 2010, **2**, 458–467.
134 L. L. del Mercato, M. M. Ferraro, F. Baldassarre, S. Mancarella, V. Greco, R. Rinaldi and S. Leporatti, *Adv. Colloid Interface Sci.*, 2014, **207**, 139–154.
135 J. Li, B. V. Parakhonskiy and A. G. Skirtach, *Chem. Commun.*, 2023, **59**, 807–835.
136 L. L. del Mercato, A. Z. Abbasi and W. J. Parak, *Small*, 2011, **3**, 351–363.
137 P. R. Gil, M. Nazarenus, S. Ashraf and W. J. Parak, *Small*, 2012, **8**, 943–948.
138 M. De Luca, M. M. Ferraro, R. Hartmann, P. Rivera-Gil, A. Klingl, M. Nazarenus, A. Ramirez, W. J. Parak, C. Bucci, R. Rinaldi and L. L. Del Mercato, *ACS Appl. Mater. Interfaces*, 2015, **7**, 15052–15060.
139 I. L. Moldero, A. Chandra, M. Cavo, C. Mota, D. Kapsokalyvas, G. Gigli, L. Moroni and L. L. del Mercato, *Small*, 2020, **16**, 2002258.

140 A. Chandra, S. Prasad, F. Alemanno, M. De Luca, R. Rizzo, R. Romano, G. Gigli, C. Bucci, A. Barra and L. L. del Mercato, *ACS Appl. Mater. Interfaces*, 2022, **14**, 18133–18149.

141 P. Srivastava, I. Tavernaro, L. Scholtz, C. Genger, P. Welker, F. Schreiber, K. Meyer and U. R. Genger, *Sci. Rep.*, 2023, **13**, 1–16.

142 G. Fan, L. Yang and Z. Chen, *Front. Chem. Sci. Eng.*, 2014, **8**, 405–417.

143 M. Strobl, T. Rappitsch, S. M. Borisov, T. Mayr and I. Klimant, *Analyst*, 2015, **140**, 7150–7153.

144 Y. Ni and J. Wu, *Org. Biomol. Chem.*, 2014, **12**, 3774–3791.

145 Q. Chen, J. Zhai, J. Li, Y. Wang and X. Xie, *Nano Res.*, 2022, **15**, 3471–3478.

146 A. Sebestyén, L. Kopper, T. Dankó and J. Tímár, *Pathol. Oncol. Res.*, 2021, **27**, 1–15.

147 I. Godet, S. Doctorman, F. Wu and D. M. Gilkes, *Cells*, 2022, **11**, 686.

148 Y. Wei, Y. Jiao, D. An, D. Li, W. Li and Q. Wei, *Sensors*, 2019, **19**, 3995–4033.

149 M. H. Gehlen, *J. Photochem. Photobiol., C*, 2020, **42**, 100338.

150 Y. Amao, *Microchim. Acta*, 2003, **143**, 1–12.

151 I. Dalfen and S. M. Borisov, *Anal. Bioanal. Chem.*, 2022, **414**, 4311–4330.

152 M. Quaranta, S. M. Borisov and I. Klimant, *Bioanal. Rev.*, 2012, **4**, 115–157.

153 M. Mital and Z. Ziora, *Coord. Chem. Rev.*, 2018, **375**, 434–458.

154 H. Xu, J. W. Aylott, R. Kopelman, T. J. Miller and M. A. Philbert, *Anal. Chem.*, 2001, **73**, 4124–4133.

155 Y. Amao and I. Okura, *J. Porphyrins Phthalocyanines*, 2009, **13**, 1111–1122.

156 C. Wu, B. Bull, K. Christensen and J. McNeill, *Angew. Chem., Int. Ed.*, 2009, **48**, 2741–2745.

157 X.-H. Wang, H. Peng and Z. Chang, *Microchim. Acta*, 2012, **178**, 147–152.

158 R. Xu, Y. Wang, X. Duan, K. Lu, D. Micheroni, A. Hu and W. Lin, *J. Am. Chem. Soc.*, 2016, **138**, 2158–2161.

159 J. Meng, X. Liu, C. Niu, Q. Pang, J. Li, F. Liu, Z. Liu and L. Mai, *Chem. Soc. Rev.*, 2020, **49**, 3142–3186.

160 Z. Luo, S. Fan, C. Gu, W. Liu, J. Chen, B. Li and J. Liu, *Curr. Med. Chem.*, 2018, **26**, 3341–3369.

161 G. A. Udourioh, M. M. Solomon, C. O. Matthews-Amune, E. I. Epelle, J. A. Okolie, V. E. Agbazue and U. Onyenze, *React. Chem. Eng.*, 2023, **8**, 278–310.

162 Y. Wen, S. Zhang, W. Yuan, W. Feng and F. Li, *Anal. Chem.*, 2023, **95**, 2478–2486.

163 S. Duanghathaipornsuk, E. J. Farrell, A. C. Alba-Rubio, P. Zelenay and D. S. Kim, *Biosensors*, 2021, **11**, 1–41.

164 H. Guo, H. Aleyasin, B. C. Dickinson, R. E. Haskew-Layton and R. R. Ratan, *Cell Biosci.*, 2014, **4**, 1–10.

165 D. Srikun, E. W. Miller, D. W. Domaille and C. J. Chang, *J. Am. Chem. Soc.*, 2008, **130**, 4596–4597.

166 Y. Kim, H. S. Kim, Y. Yang, K. Baek, N. Choi and M. H. Park, *J. Toxicol. Environ. Health Sci.*, 2017, **9**, 108–115.

167 G. Kim, Y. E. L. Koo, H. Xu, M. A. Philbert and R. Kopelman, *Anal. Chem.*, 2010, **82**, 2165–2169.

168 L. I. Kazakova, L. I. Shabarchina, S. Anastasova, A. M. Pavlov, P. Vadgama, A. G. Skirtach and G. B. Sukhorukov, *Anal. Bioanal. Chem.*, 2013, **405**, 1559–1568.

169 K. G. de la Cruz-López, L. J. Castro-Muñoz, D. O. Reyes-Hernández, A. García-Carrancá and J. Manzo-Merino, *Front. Oncol.*, 2019, **9**, 1–21.

170 B. Phypers and J. M. T. Pierce, *Contin. Educ. Anaesth., Crit. Care Pain*, 2006, **6**, 128–132.

171 S. Liu, J. Zhao, K. Zhang, L. Yang, M. Sun, H. Yu, Y. Yan, Y. Zhang, L. Wu and S. Wang, *Analyst*, 2016, **141**, 2296–2302.

172 V. G. Deepagan, E. K. Pramod Kumar, Y. D. Suh and J. H. Park, *Macromol. Res.*, 2018, **26**, 577–580.

173 Q. Pan, X. Deng, W. Gao, J. Chang, Y. Pu and B. He, *Colloids Surf., B*, 2020, **194**, 111223.

174 K. Rajes, K. A. Walker, S. Hadam, F. Zabihi, J. Ibrahim-Bacha, G. Germer, P. Patoka, B. Wassermann, F. Rancan, E. Rühl, A. Vogt and R. Haag, *ACS Biomater. Sci. Eng.*, 2021, **7**, 2485–2495.

175 C. Feng, F. Wang, Y. Dang, Z. Xu, H. Yu and W. Zhang, *Langmuir*, 2017, **33**, 3287–3295.

176 J. Zhou, R. Zhao, Y. Du, S. Liu, W. Li, S. Gai, F. He, L. Feng and P. Yang, *Adv. Funct. Mater.*, 2022, **32**, 2112083.

177 F. Liu, T. Bing, D. Shangguan, M. Zhao and N. Shao, *Anal. Chem.*, 2016, **88**, 10631–10638.

178 M. Sheth and L. Esfandiari, *Front. Oncol.*, 2022, **12**, 1–15.

179 M. Wei, P. Lin, Y. Chen, J. Y. Lee, L. Zhang, F. Li and D. Ling, *Nanomedicine*, 2020, **15**, 2871–2881.

180 M. L. Valentine, A. E. Cardenas, R. Elber and C. R. Baiz, *Biophys. J.*, 2018, **115**, 1541–1551.

181 R. M. Paredes, J. C. Etzler, L. T. Watts, W. Zheng and J. D. Lechleiter, *Methods*, 2008, **46**, 143–151.

182 D. Si, T. Epstein, Y. E. Koo Lee and R. Kopelman, *Anal. Chem.*, 2012, **84**, 978–986.

183 Y. Lin, Y. Zheng, Y. Guo, Y. Yang, H. Li, Y. Fang and C. Wang, *Sens. Actuators, B*, 2018, **273**, 1654–1659.

184 A. Schulz, R. Woolley, T. Tabarin and C. McDonagh, *Analyst*, 2011, **136**(8), 1722.

185 G. Gao, Y. Cao, W. Liu, D. Li, W. Zhou and J. Liu, *Anal. Methods*, 2017, **9**, 5570–5579.

186 S. Dietrich, S. E. Stanca, C. G. Cranfield, B. Hoffmann, K. Benndorf and C. Biskup, in *Multiphoton Microscopy in the Biomedical Sciences X*, ed. A. Periasamy, P. T. C. So and K. König, SPIE BiOS, San Francisco, California, United States, 2010, vol. 756914, p. 756914.

187 R. Wang, X. Du, Y. Wu, J. Zhai and X. Xie, *ACS Sens.*, 2018, **3**, 2408–2414.

188 X. Xie, G. A. Crespo and E. Bakker, *Anal. Chem.*, 2013, **85**, 7434–7440.

189 J. M. David and A. K. Rajasekaran, *J. Kidney Cancer VHL*, 2015, **2**, 15–24.

190 D. Kwon, E. Park, H. Sesaki and S. Kang, *Biochem. Biophys. Res. Commun.*, 2017, **493**, 737–743.

191 M. Zacchia and L. Abategiovanni, *Kidney Dis.*, 2016, **2**, 72–79.

192 T. S. Rimmele and J.-Y. Chatton, *PLoS One*, 2014, **9**, 1–9.

193 J. Liu, L. Pan, C. Shang, B. Lu, R. Wu, Y. Feng, W. Chen, R. Zhang, J. Bu, Z. Xiong and W. Bu, *Sci. Adv.*, 2020, **6**, 1–11.
194 S. Wilhelm, *ACS Nano*, 2017, **11**, 10644–10653.
195 B. Andersson and V. Janson, *Toxicol. In Vitro*, 2006, **20**, 986–994.
196 J. Liu, F. Li, Y. Wang, L. Pan, P. Lin, B. Zhang, K. Shin, D. Kim, S. Jang, H. J. Chung, H. Tian and Q. Wang, *Nat. Nanotechnol.*, 2020, **15**, 321–330.
197 T. T. Ruckh, C. G. Skipwith, W. Chang, A. W. Senko, V. Bulovic, P. O. Anikeeva and H. A. Clark, *ACS Nano*, 2016, **10**, 4020–4030.
198 N. Shcheynikov, A. Son, J. Hee, O. Yamazaki, E. Ohana and I. Kurtz, *Proc. Natl. Acad. Sci. U. S. A.*, 2015, **5**, E329–E337.
199 M. J. Ruedas-Rama, A. Orte, E. A. H. Hall, J. M. Alvarez-Pez and E. M. Talavera, *Analyst*, 2012, **137**, 1500–1508.
200 Y. Wang, H. Mao and L. B. Wong, *Nanotechnology*, 2010, **21**, 055101.
201 N. L. Henry and D. F. Hayes, *Mol. Oncol.*, 2012, **6**, 140–146.
202 S. Hosseini, P. Vázquez-Villegas, M. Rito-Palomares and S. O. Martinez-Chapa, *Enzyme-linked Immunosorbent Assay (ELISA)*, Springer Singapore, Singapore, 2018.
203 M. T. Rahman, M. S. Uddin, R. Sultana, A. Moue and M. Setu, *Anwer Khan Mod. Med. Coll. J.*, 2013, **4**, 30–36.
204 U. Laraib, S. Sargazi, A. Rahdar, M. Khatami and S. Pandey, *Int. J. Biol. Macromol.*, 2022, **195**, 356–383.
205 D. A. Murphy and S. A. Courtneidge, *Nat. Rev. Mol. Cell Biol.*, 2011, **12**, 413–426.
206 R. Ferrari, G. Martin, O. Tagit, A. Guichard, A. Cambi, R. Voituriez, S. Vassilopoulos and P. Chavrier, *Nat. Commun.*, 2019, **10**, 1–15.
207 Y. Wang, P. Shen, C. Li, Y. Wang and Z. Liu, *Anal. Chem.*, 2012, **84**, 1466–1473.
208 X. He, J. Gao, S. S. Gambhir and Z. Cheng, *Trends Mol. Med.*, 2010, **16**, 574–583.
209 M. Swierczewska, S. Lee and X. Chen, *Phys. Chem. Chem. Phys.*, 2011, **13**, 9929–9941.
210 E. Hutter and D. Maysinger, *Trends Pharmacol. Sci.*, 2013, **34**, 497–507.
211 S. Lee, E. J. Cha, K. Park, S. Y. Lee, J. K. Hong, I. C. Sun, S. Y. Kim, K. Choi, I. C. Kwon, K. Kim and C. H. Ahn, *Angew. Chem., Int. Ed.*, 2008, **47**, 2804–2807.
212 S. Lee, J. H. Ryu, K. Park, A. Lee, S. Y. Lee, I. C. Youn, C. H. Ahn, S. M. Yoon, S. J. Myung, D. H. Moon, X. Chen, K. Choi, I. C. Kwon and K. Kim, *Nano Lett.*, 2009, **9**, 4412–4416.
213 L. Yin, H. Sun, M. Zhao, A. Wang, S. Qiu, Y. Gao, J. DIng, S. J. Ji, H. Shi and M. Gao, *J. Org. Chem.*, 2019, **84**, 6126–6133.
214 T. Ma, Y. Hou, J. Zeng, C. Liu, P. Zhang, L. Jing, D. Shangguan and M. Gao, *J. Am. Chem. Soc.*, 2018, **140**, 211–218.
215 C. D. Belair, T. R. Yeager, P. M. Lopez and C. A. Reznikoff, *Proc. Natl. Acad. Sci. U. S. A.*, 1997, **94**, 13677–13682.
216 J. Vinagre, V. Pinto, R. Celestino, M. Reis, H. Pópulo, P. Boaventura, M. Melo, T. Catarino, J. Lima, J. M. Lopes, V. Máximo, M. Sobrinho-Simões and P. Soares, *Virchows Arch.*, 2014, **465**, 119–133.
217 D. Ma, H. Bai, J. Li, Y. Li, L. Song, J. Zheng and C. Miao, *Anal. Bioanal. Chem.*, 2022, **414**, 1891–1898.
218 K. Clack, N. Soda, S. Kasetsirikul, R. G. Mahmudunnabi, N.-T. Nguyen and M. J. A. Shiddiky, *Small*, 2023, **1**, 2205856.
219 S. Singh, P. S. Podder, M. Russo, C. Henry and S. Cinti, *Lab Chip*, 2023, **23**, 44–61.
220 Z. Sun, J. Li, Y. Yang, Y. Tong, H. Li, C. Wang, L. Du and Y. Jiang, *Bioconjugate Chem.*, 2022, **33**, 1698–1706.
221 J. Gao, X. Yu, X. Wang, Y. He and J. Ding, *Engineering*, 2022, **13**, 31–45.
222 M. Cavo, F. Serio, N. R. Kale, E. D'Amone, G. Gigli and L. L. del Mercato, *Biomater. Sci.*, 2020, **8**, 4887.
223 A. Accardo, M. Ventre, C. Chiappini, V. Onesto, M. L. Coluccio, P. Netti and F. Gentile, in *Neural Regenerative Nanomedicine*, Elsevier, 2020, pp. 47–88.
224 F. Serio, N. Silvestri, S. Kumar, G. E. P. Nucci, S. Nitti, V. Onesto, F. Catalano, E. D. Amone, G. Gigli, L. Loretta and T. Pellegrino, *J. Colloid Interface Sci.*, 2022, **607**, 34–44.
225 E. Hendrick, M. Frey, E. Herz and U. Wiesner, *J. Eng. Fibers Fabr.*, 2010, **5**, 21–30.
226 B. Y. Chen, C. C. Kuo, Y. S. Huang, S. T. Lu, F. C. Liang and D. H. Jiang, *ACS Appl. Mater. Interfaces*, 2015, **7**, 2797–2808.
227 L. L. del Mercato, M. Moffa, R. Rinaldi and D. Pisignano, *Small*, 2015, **11**, 6417–6424.
228 V. Onesto, S. Forciniti, F. Alemanno, K. Narayanankutty, A. Chandra, S. Prasad, A. Azzariti, G. Gigli, A. Barra, A. De Martino, D. De Martino and L. L. del Mercato, *ACS Nano*, 2023, **17**, 3313–3323.
229 A. Mahmood, D. Patel, B. Hickson, J. Desrochers and X. Hu, *Int. J. Mol. Sci.*, 2022, **23**, 1415.
230 G. Schuszter, T. Gehèr-Herczegh, A. Szucs, A. Toth and D. Horvath, *Phys. Chem. Chem. Phys.*, 2017, **19**, 12136–12143.
231 R. Rizzo, V. Onesto, G. Morello, H. Iuele, F. Scalera, S. Forciniti, G. Gigli, A. Polini, F. Gervaso and L. L. del Mercato, *Mater. Today Bio*, 2023, **20**, 100655.
232 R. Rizzo, V. Onesto, S. Forciniti, A. Chandra, S. Prasad, H. Iuele, F. Colella, G. Gigli and L. L. del Mercato, *Biosens. Bioelectron.*, 2022, **212**, 114401.
233 P. Chiarugi and P. Cirri, *Cancer Lett.*, 2016, **380**, 272–280.
234 A. Chandra and N. Singh, *Chem. Commun.*, 2018, **54**, 1643–1646.
235 D. B. Longley, D. P. Harkin and P. G. Johnston, *Nat. Rev. Cancer*, 2003, **3**, 330–338.
236 A. Delic, E. Mariussen, D. Roede and A. Krivokapic, *Chempluschem*, 2021, **86**, 176–183.
237 F. Li, Y. Liu, Y. Xu, Y. Li, J. Liu, M. Lv, C. Ruan, H. Pan and X. Zhao, *ACS Omega*, 2020, **5**, 19796–19804.
238 Y. Ando, H. P. Ta, D. P. Yen, S. Lee, S. Raola and K. Shen, *Sci. Rep.*, 2017, **7**, 15233.
239 R. L. Wilson, J. P. Connell and K. J. Grande-allen, *ACS Biomater. Sci. Eng.*, 2019, **5**, 4522–4230.
240 M. F. Wesseler, M. N. Johansen, A. Kızıltay, K. I. Mortensen and N. B. Larsen, *Lab Chip*, 2022, **22**, 4167–4179.
241 A. Fedi, C. Vitale, P. Giannoni, G. Caluori and A. Marrella, *Sensors*, 2022, **22**, 1517.

242 I. L. Moldero, A. Chandra, M. Cavo, C. Mota, D. Kapsokalyvas, G. Gigli, L. Moroni and L. L. del Mercato, *Small*, 2020, **16**, 2002258.
243 S. Hernot, L. van Manen, P. Debie, J. S. D. Mieog and A. L. Vahrmeijer, *Lancet Oncol.*, 2019, **20**, e354–e367.
244 M. Koch and V. Ntziachristos, *Annu. Rev. Med.*, 2016, **67**, 153–164.
245 J. S. D. Mieog, F. B. Achterberg, A. Zlitni, M. Hutteman, J. Burggraaf, R. J. Swijnenburg, S. Gioux and A. L. Vahrmeijer, *Nat. Rev. Clin. Oncol.*, 2022, **19**, 9–22.
246 S. Van Keulen, M. Hom, H. White, E. L. Rosenthal and F. M. Baik, *Mol. Imaging Biol.*, 2023, **25**, 36–45.
247 K. Wang, Y. Du, Z. Zhang, K. He, Z. Cheng, L. Yin, D. Dong, C. Li, W. Li, Z. Hu, C. Zhang, H. Hui, C. Chi and J. Tian, *Nat. Rev. Bioeng.*, 2023, **1**, 161–179.
248 X. Zhou, Y. Liu, Q. Liu, L. Yan, M. Xue, W. Yuan, M. Shi, W. Feng, C. Xu and F. Li, *Theranostics*, 2019, **9**, 4597–4607.
249 J. T. Unkart, S. L. Chen, I. L. Wapnir, J. E. González, A. Harootunian and A. M. Wallace, *Ann. Surg. Oncol.*, 2017, **24**, 3167–3173.
250 M. I. Khan, M. I. Hossain, M. K. Hossain, M. H. K. Rubel, K. M. Hossain, A. M. U. B. Mahfuz and M. I. Anik, *ACS Appl. Bio Mater.*, 2022, **5**, 971–1012.
251 E. Thankarajan, S. Jadhav, G. Luboshits, G. Gellerman and L. Patsenker, *Anal. Chem.*, 2021, **93**, 8265–8272.
252 T. M. Ebaston, A. Rozovsky, A. Zaporozhets, A. Bazylevich, H. Tuchinsky, V. Marks, G. Gellerman and L. D. Patsenker, *ChemMedChem*, 2019, **14**, 1727–1734.
253 L. Patsenker and G. Gellerman, *Isr. J. Chem.*, 2020, **60**, 504–518.
254 A. Rozovsky, T. M. Ebaston, A. Zaporozhets, A. Bazylevich, H. Tuchinsky, L. Patsenker and G. Gellerman, *RSC Adv.*, 2019, **9**, 32656–32664.